J. Fluid Mech. (1983), *vol.* 130, *pp.* 411–452
Printed in Great Britain

Small-scale structure of the Taylor–Green vortex

By MARC E. BRACHET†, DANIEL I. MEIRON,
STEVEN A. ORSZAG,
Massachusetts Institute of Technology, Cambridge, MA 02139

B. G. NICKEL,
University of Guelph, Guelph, Ontario

RUDOLF H. MORF
R.C.A. Laboratories, Zurich, Switzerland

AND URIEL FRISCH
CNRS, Observatoire de Nice, 06-Nice, France

(Received 5 February 1982 and in revised form 14 June 1982)

The dynamics of both the inviscid and viscous Taylor–Green (TG) three-dimensional vortex flows are investigated. This flow is perhaps the simplest system in which one can study the generation of small scales by three-dimensional vortex stretching and the resulting turbulence. The problem is studied by both direct spectral numerical solution of the Navier–Stokes equations (with up to 256^3 modes) and by power-series analysis in time.

The *inviscid* dynamics are strongly influenced by symmetries which confine the flow to an impermeable box with stress-free boundaries. There is an early stage during which the flow is strongly anisotropic with well-organized (laminar) small-scale excitation in the form of vortex sheets located near the walls of this box. The flow is smooth but has complex-space singularities within a distance $\hat{\delta}(t)$ of real (physical) space which give rise to an exponential tail in the energy spectrum. It is found that $\hat{\delta}(t)$ decreases exponentially in time to the limit of our resolution. Indirect evidence is presented that more violent vortex stretching takes place at later times, possibly leading to a real singularity ($\hat{\delta} = 0$) at a finite time. These direct integration results are consistent with new temporal power-series results that extend the Morf, Orszag & Frisch (1980) analysis from order t^{44} to order t^{80}. Still, convincing evidence for or against the existence of a real singularity will require even more sophisticated analysis. The *viscous* dynamics (decay) have been studied for Reynolds numbers R (based on an integral scale) up to 3000 and beyond the time $t_{\max}$ at which the maximum energy dissipation is achieved. Early-time, high-R dynamics are essentially inviscid and laminar. The inviscidly formed vortex sheets are observed to roll up and are then subject to instabilities accompanied by reconnection processes which make the flow increasingly chaotic (turbulent) with extended high-vorticity patches appearing away from the impermeable walls. Near $t_{\max}$ the small scales of the flow are nearly isotropic provided that $R \gtrsim 1000$. Various features characteristic of fully developed turbulence are observed near $t_{\max}$ when $R = 3000$ and $R_\lambda = 110$:

(i) a k^{-n} inertial range in the energy spectrum is obtained with $n \approx 1.6$–2.2 (in contrast with a much steeper spectrum at earlier times);

† Present address: CNRS, Observatoire de Nice, 06-Nice, France.

(ii) the energy dissipation has considerable spatial intermittency; its spectrum has a $k^{-1+\mu}$ inertial range with the codimension $\mu \approx 0.3$–0.7.

Skewness and flatness results are also presented.

1. Introduction

The fundamental dynamical mechanism involved in homogeneous three-dimensional turbulent flows is the enhancement of vorticity by vortex-line stretching and the consequent production of small-scale eddies. This process controls the turbulent-energy dynamics and hence the global structure and evolution of the flow. A prototype of this process is given by the Taylor–Green vortex (Taylor & Green 1937; denoted as TG below), which is perhaps the simplest system in which to study the generation of small scales and the resulting turbulence.

The generalized TG vortex is that three-dimensional incompressible flow that develops from the single-mode initial condition†

$$\left.\begin{aligned} v_x(\boldsymbol{r}, t=0) &= \frac{2}{\sqrt{3}} \sin\left(\theta + \frac{2\pi}{3}\right) \sin x \cos y \cos z, \\ v_y(\boldsymbol{r}, t=0) &= \frac{2}{\sqrt{3}} \sin\left(\theta - \frac{2\pi}{3}\right) \cos x \sin y \cos z, \\ v_z(\boldsymbol{r}, t=0) &= \frac{2}{\sqrt{3}} \sin\theta \cos x \cos y \sin z. \end{aligned}\right\} \tag{1.1}$$

The flow discussed at length in this paper is that for which $\theta = 0$ in (1.1). In this case the initial flow has two-dimensional streamlines, but the flow is three-dimensional for all $t > 0$. We have made a preliminary study of the flow developing from (1.1) with $\theta = \frac{1}{2}\pi$, corresponding to an initially highly symmetric flow, which suggests no particular advantage over the TG choice $\theta = 0$ for the study of small-scale turbulence at late times.

The flows that develop from the initial condition (1.1) have the Fourier representation (Orszag 1974)

$$v_x(\boldsymbol{r}, t) = \sum_{m=0}^{\infty} \sum_{n=0}^{\infty} \sum_{p=0}^{\infty} u_x(m, n, p, t) \sin mx \cos ny \cos pz, \tag{1.2a}$$

$$v_y(\boldsymbol{r}, t) = \sum_{m=0}^{\infty} \sum_{n=0}^{\infty} \sum_{p=0}^{\infty} u_y(m, n, p, t) \cos mx \sin ny \cos pz, \tag{1.2b}$$

$$v_z(\boldsymbol{r}, t) = \sum_{m=0}^{\infty} \sum_{n=0}^{\infty} \sum_{p=0}^{\infty} u_z(m, n, p, t) \cos mx \cos ny \sin pz, \tag{1.2c}$$

where $\boldsymbol{u}(m, n, p, t)$ vanishes unless m, m, p are either all even or all odd integers. The representation (1.2) is the basis for much of the ensuing analysis. The many symmetries of the TG vortex flow (see appendix A) can be verified from (1.2).

In the past this flow has been used to study such questions as: (i) enhancement of vorticity by vortex line stretching (TG); (ii) approach to isotropy of the small scales (Orszag 1974); (iii) possible singular behaviour of solutions of the Euler equations (Morf, Orszag & Frisch 1980, denoted as MOF below); and (iv) high-Reynolds-number behaviour of energy dissipation (Orszag 1974).

In the present work we report additional studies of this flow, including new results

† This initial condition differs from that of previous investigators, including TG and Morf, Orszag & Frisch (1980), by a shift of origin. It offers the advantage of the symmetric Fourier representation (1.2).

concerning: (i) the character of the inviscid flow; (ii) the analytic structure of the inviscid flow and the time development of energy spectra; (iii) analysis of high-Reynolds-number behaviour including results on the formation of an inertial range; (iv) analysis of the geometry of the regions of high vorticity and, especially, of their intermittency; and (v) possible differences between viscous and inviscid behaviours. In particular, we are able to report the first numerically computed three-dimensional inertial range which, although crude by experimental standards, is obtained directly from the Navier–Stokes equations without any turbulence modelling or other *ad hoc* hypotheses.

It has been estimated (Orszag 1976) that a computation of an inertial range like that observed in the high-Reynolds-number tidal-channel experiment of Grant, Stewart & Moilliet (1962) would be far beyond the power of both available and presently foreseeable computers. The present work has been possible because of the development of new algorithms that take advantage of the symmetries of the TG flow (see appendix C). It has allowed us to reach a range of scales and Reynolds numbers where scaling behaviour characteristic of fully developed turbulence begins to be manifested.

In §2, we describe heuristically the early-time evolution of the inviscid flow. Then the quantitative behaviour of the inviscid flow is discussed using direct numerical solutions of the Navier–Stokes equations (§3) and series-analysis methods (§4). In §5, the character of the viscous flows is analysed, including such diagnostics as energy spectra. In §6, the nature of intermittency and dissipative structures in the flow is investigated. Finally, in §7 we discuss the appearance of spatial chaos in the high-Reynolds-number flow. Some details of our methods are discussed in the appendices.

2. Early-time behaviour of the inviscid flow

The symmetries of the TG vortex are listed in appendix A. Here we emphasize only those that help to visualize the qualitative features of the flow and those that may be important in making this flow atypical of general three-dimensional flow. First, for all times, no fluid crosses any of the boundaries x, y or $z = n\pi$, where n is an integer. Therefore the flow can be visualized as flow in the box $0 \leqslant x, y, z \leqslant \pi$ with impermeable stress-free faces. In the following discussion, the region $0 \leqslant x, y, z \leqslant \pi$ is termed the *impermeable box*, as it confines the flow, while the region $0 \leqslant x, y, z \leqslant 2\pi$ is termed the *periodicity box*, as it reflects the periodicity of the Fourier series (1.2). Also, because of the symmetries listed in appendix A, the flow at any point in space can be inferred from its values in the *fundamental box* $0 \leqslant x, y, z \leqslant \frac{1}{2}\pi$.

Secondly, if near each face we write the velocity field in terms of components parallel or perpendicular to the face, i.e. $\boldsymbol{v} = \boldsymbol{v}_{\parallel} + \boldsymbol{v}_{\perp}$, then $\boldsymbol{v}_{\perp}$ and $\partial \boldsymbol{v}_{\parallel}/\partial n$ vanish on the face. This implies that the vorticity on each face is normal to that face so it may be written $\boldsymbol{\omega} = \zeta \hat{\boldsymbol{n}}$, where $\hat{\boldsymbol{n}}$ is the unit normal. Note that ζ must vanish on all edges of the box where faces meet. In contrast, a general incompressible flow will have only isolated points of vanishing vorticity. (Both velocity and vorticity also vanish for all time at the centre $x = y = z = \frac{1}{2}\pi$.)

Thirdly, the vanishing of $\boldsymbol{v}_{\perp}$ and $\partial \boldsymbol{v}_{\parallel}/\partial n$ on each face also implies that the tensor $\boldsymbol{\nabla v}$ is partly diagonal. One principal axis of the strain rate or symmetric part of this tensor is then perpendicular to the face. Furthermore, the magnitude of the strain rate along this axis determines the fractional growth rate of the normal vorticity on the face, i.e.

$$\frac{\partial \boldsymbol{v}_{\perp}}{\partial n} = -\boldsymbol{\nabla} \cdot \boldsymbol{v}_{\parallel} = \frac{\mathrm{d}}{\mathrm{d}t} \ln |\zeta|. \tag{2.1}$$

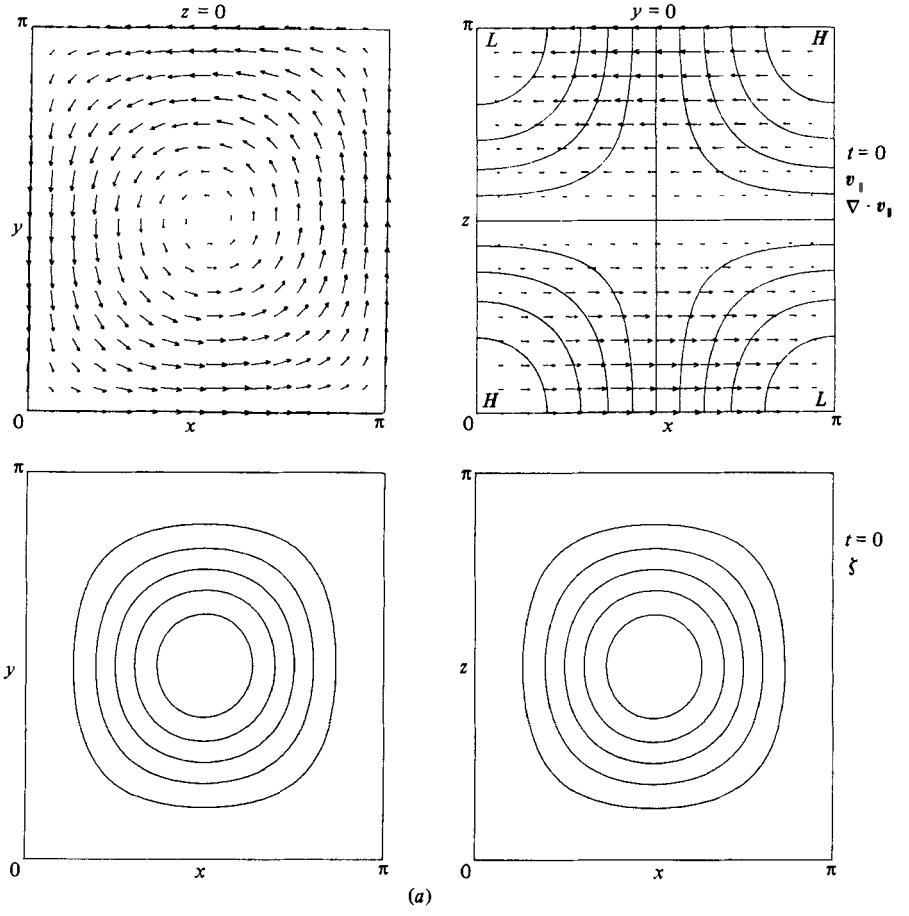

(a)

FIGURE 1(a). For caption see facing page.

Here and in the remainder of this section, zero viscosity is assumed. It follows from (2.1) that ζ, on each face, satisfies the local conservation law

$$\frac{\partial \zeta}{\partial t} + \nabla \cdot (\boldsymbol{v}_{\parallel} \zeta) = 0, \tag{2.2}$$

and the global conservation law $\int \zeta \, \mathrm{d}A = \text{constant}$. Also, ζ at $t = 0$ vanishes only on the edges. Therefore the sign of the conserved quantity ζ is a constant of motion.

Fourthly, there are global restrictions on the TG flow that are quite special. For example, the total helicity $\int \boldsymbol{v} \cdot \boldsymbol{\omega} \, \mathrm{d}\boldsymbol{x}$ vanishes for all time. Also, the vortex lines, defined by $\mathrm{d}\boldsymbol{x}/\mathrm{d}s = \boldsymbol{\omega}(\boldsymbol{x}(s), t)$, are closed and unknotted curves in the inviscid flow. General three-dimensional flow leaves room for considerably more complicated topologies (see §7).

Most of our discussion of the real-space dynamics will be confined to the flow on and near the faces of the impermeable box, which by symmetry need only be the bottom face, $z = 0$, and one of the side faces, say $y = 0$. Indeed, computation of the flow shows that most of the 'action' in the flow for early-to-moderate times ($t \lesssim 4$) occurs near these faces.

Simple dynamical considerations determine the qualitative features of the flow on the faces of the impermeable box. In particular, the initial vortex on the bottom face is forced by centrifugal action to spiral outwards toward the edges and then up the

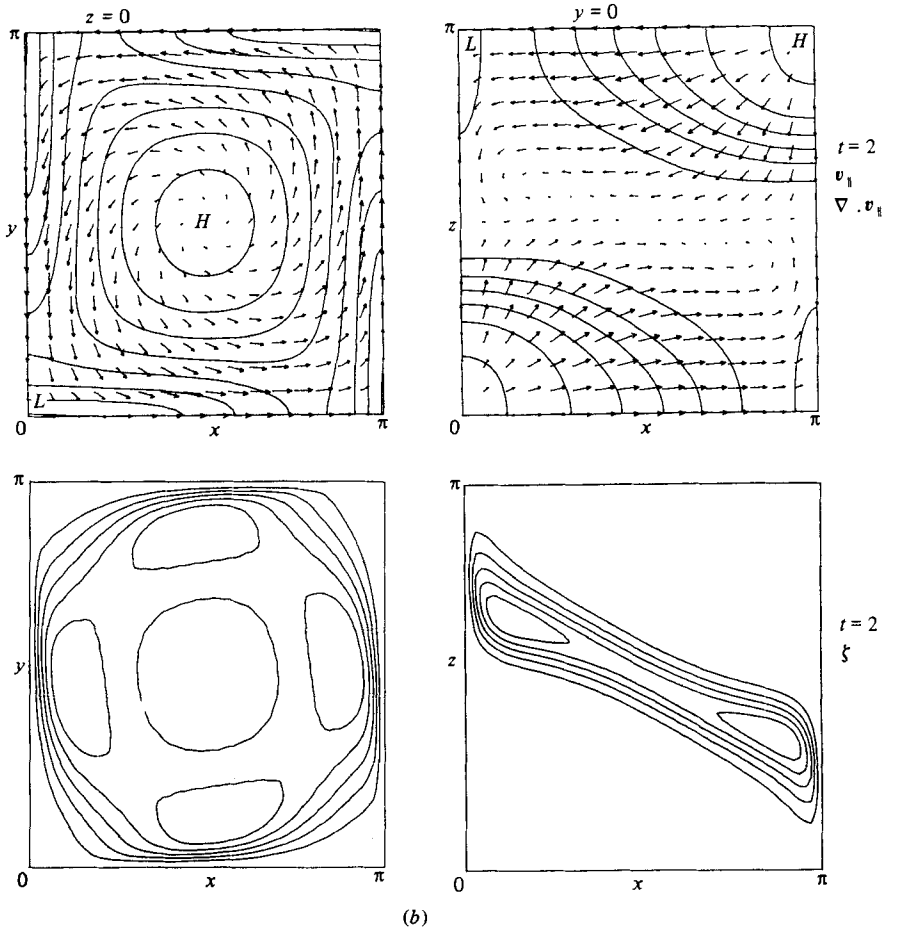

FIGURE 1. A plot of the velocity and vorticity at $t = 0$ (*a*) and $t = 2$ (*b*) on the $y = 0$ and $z = 0$ faces of the impermeable cube of the inviscid TG vortex. Vectors indicate the velocity field (which lies in the plane of the plot) while solid lines are contours of constant strain rate $\nabla \cdot \boldsymbol{v}_\parallel$ and total vorticity ω^2, as indicated in the figure. The initial vorticity on the $z = 0$ plane is $\zeta(t = 0) = 2 \sin x \sin y$; it decays at the centre of this face from its value $\zeta = 2$ at $t = 0$ to $\zeta = 0.8$ at $t = 2$. On this face $\omega^2 = \zeta^2$; contours are equally spaced in ω^2. On the $y = 0$ face the initial vorticity is $\zeta = \sin x \sin z$; its value at the centre grows from $\zeta = 1$ at $t = 0$ to $\zeta = 1.7$ at $t = 2$. The strain rate $\nabla \cdot \boldsymbol{v}_\parallel$ on the $z = 0$ face has changed from identically zero at $t = 0$ to a low of -0.833 at the corners and a high of 0.723 at the centre at $t = 2$. On the $y = 0$ face the strain rate changes from $-1 \leqslant \nabla \cdot \boldsymbol{v}_\parallel \leqslant 1$ at $t = 0$ to $-1.75 \leqslant \nabla \cdot \boldsymbol{v}_\parallel \leqslant 0.94$ at $t = 2$. The centre of the $y = 0$ face has become a point of convergence, $-\nabla \cdot \boldsymbol{v}_\parallel = 0.53$ at $t = 2$. The labels L and H indicate lows and highs respectively of $\nabla \cdot \boldsymbol{v}_\parallel$.

side faces (see figure 1).† The initial vorticity maximum at the centre of the bottom face decreases in time because of the consequent horizontal divergence of the flow (see (2.1)). New vorticity maxima appear close to the edges, where they build up dramatically because of the large strain-rate tensor there. (The vorticity must remain zero at the edges, but large gradients are not excluded.) A corresponding outflow on the top face and downflow from the top edges onto the side faces leads to a convergence of fluid near the horizontal centreline of each side face, from where it is forced back into the centre of the box and subsequently back to the top and bottom

† Without pressure effects and/or the z-variation of the initial conditions (1.1), the initially two-dimensional TG flow would remain two-dimensional for all time.

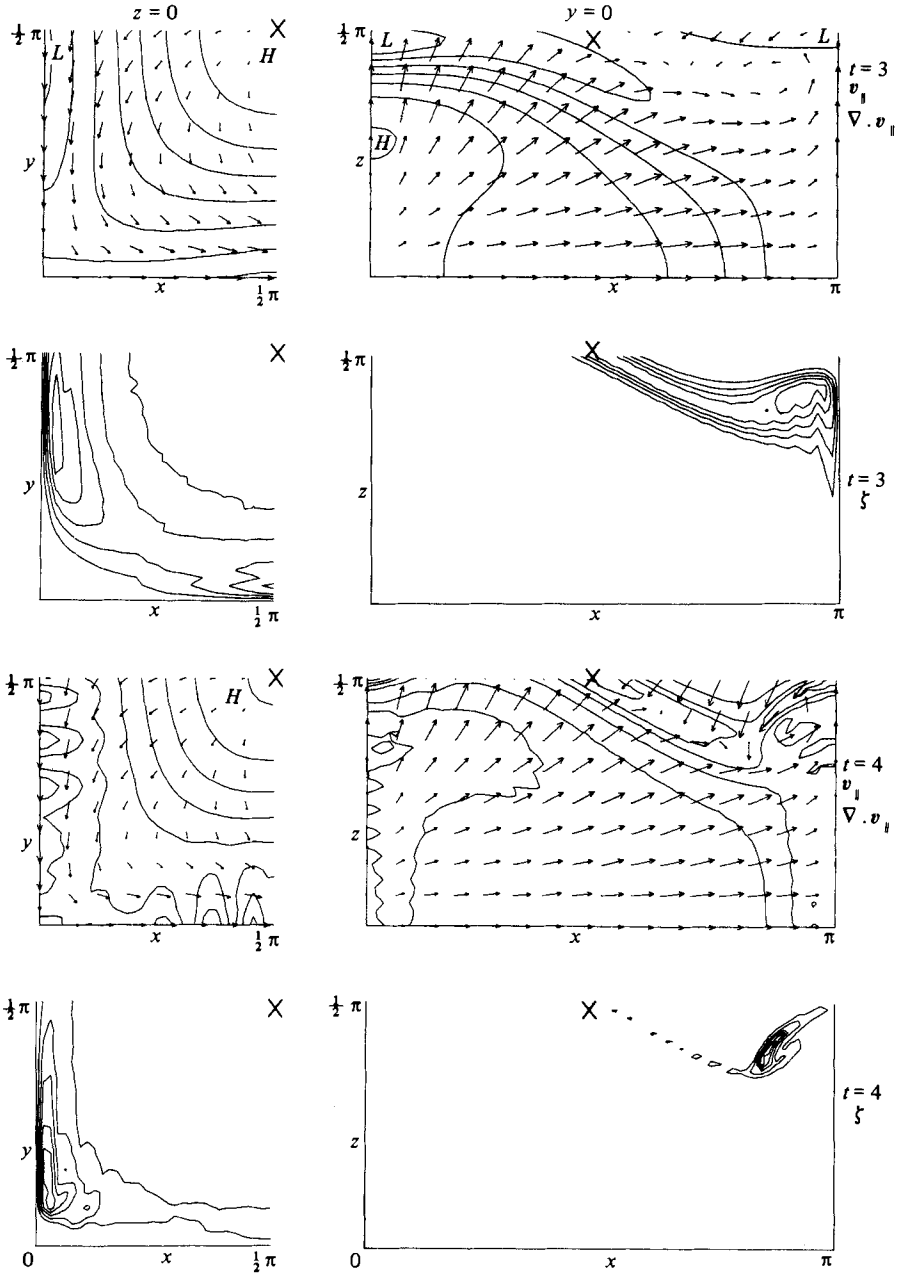

FIGURE 2. Velocity fields and contours of constant $\nabla \cdot \boldsymbol{v}_{\parallel}$ and ω^2 for the inviscid TG vortex at $t = 3$ and 4. Only portions of the $z = 0$ and $y = 0$ plane are shown; the flow in the remaining areas can be obtained by rotation about the centre of the faces indicated by the large crosses. The divergence $\nabla \cdot \boldsymbol{v}_{\parallel}$ at the centre of the $z = 0$ face continues to grow; it reaches 0.82 at $t = 3$ and 0.841 at $t = 4$. Similarly, the convergence at the centre of the $y = 0$ face increases to 1.09 at $t = 3$ and 4.17 at $t = 4$. Because of the choice of level curves, a very narrow vortex sheet running through the centre of the $y = 0$ face has been lost from view at $t = 4$.

faces. The vorticity on the side faces is efficiently produced in the zone of convergence, and builds up rapidly into a vortex sheet (see figure 2). A simple model of this phenomenon is given in appendix D.

These considerations determine the dominant features of the flow correctly for times up to about 4. Some clues to the later behaviour of the inviscid flow can be obtained just before our calculations (that use up to $256 \times 256 \times 256$ Fourier modes) lose accuracy. As may be seen from figure 2, the vortex sheet that appears in the plane $y = 0$ becomes stronger in time and apparently becomes unstable for $t \gtrsim 3$ to an instability (perhaps like Kelvin–Helmholtz instability) near $(x, z) = (0.2, 0.6)\pi$ and $(0.8, 0.4)\pi$. For t near 4, the circulatory flow that develops near these unstable regions decreases the convergence there due to centrifugal action and this forces an enhanced convergence near the plane's centre $x = z = \frac{1}{2}\pi$. We find (cf. figure 2) that the maximum strain rate $-\nabla \cdot \boldsymbol{v}_{\parallel}$ on the plane $y = 0$ increases from about 2.3 for $t \approx 3$, to about 4.7 for $t \approx 4$, showing a halving of the characteristic evolution time of the flow. As t increases beyond 4, there seem to be local vorticity maxima developing away from the walls of the impermeable box, suggesting the formation of new 'daughter' vortices in the interior and an exceedingly complicated flow structure.

In this context we note that Chorin (1981) has recently reported numerical results for the inviscid TG flow using a discrete-vortex method. Chorin finds that the vorticity blows up in a finite time and the integral of its square seems to concentrate in a set of Hausdorff codimension $\mu = 0.5$. In this strictly inviscid case, the latter is not supported by our calculations (and the former only marginally at best); it may be that Chorin's vortex scheme is actually making the flow slightly viscous (see §6).

3. Analysis of the inviscid flow: direct integration by time stepping

In §§3 and 4 we analyse the inviscid TG flow – in this § by solving the Euler equations using time-marching numerical techniques, and in §4 by analysis of high-order power series in time. First we review some earlier results. Series extrapolation methods have been applied to the TG vortex and other flows in order to study their analytic structure and to investigate the question of the existence of singularities. In particular, evidence was obtained (MOF) that initially smooth, boundary-free, inviscid three-dimensional flow may become singular after a finite time. This would imply that vorticity could be stretched an infinite amount in a finite time. MOF analysed the temporal series of the 'generalized enstrophies', defined as the spatial mean-square derivative of order λ of the velocity field,

$$\Omega_\lambda(t) = \tfrac{1}{2}\sum_{\boldsymbol{k}} |\boldsymbol{k}|^{2\lambda} |\boldsymbol{u}(\boldsymbol{k}, t)|^2 = \tfrac{1}{2}\sum_{k=0}^{\infty} t^{2r} A_\lambda^{(2r)} \tag{3.1}$$

for the inviscid TG vortex flow. The series was calculated numerically to $O(t^{44})$. This involves derivatives of the velocity field with wavenumber components k_i ranging up to $k_{\max} = 23$. The radius of convergence was found to be determined by imaginary-time singularities at $t^2 \approx -5$. Thus analytic continuation was required to study the question of the existence of a real-time singularity. Padé approximants indicated the possibility of a singularity at $t \approx 5.2$ (cf. §4).

The reliability of this method was subsequently studied for flow problems for which rigorous results are known (Morf *et al.* 1981). In particular, for the inviscid Burgers equation, series-extrapolation methods correctly predict the location and nature of the singularity that represents the formation of shock waves. Also, for two-dimensional Euler flow, series analysis does not predict a real singularity, consistent with rigorous theorems (Wolibner 1933; see also Frisch 1983).

In this section, we study the reliability of the Padé analysis by the analyticity-strip method introduced by Sulem, Sulem & Frisch (1983), which has been previously employed to analyze two-dimensional magnetohydrodynamics for the existence of real-time singularities (cf. Morf *et al.* 1981; Frisch *et al.* 1983). In this method, the time evolution of the spherically averaged energy spectrum $E(k,t)$, calculated as the band average

$$\left.\begin{aligned} E(k,t)\,\Delta k &= \tfrac{1}{2}\sum_{k\in C(k)} |\boldsymbol{u}(\boldsymbol{k}',t)|^2, \\ C(k) &= \{k' | k-\tfrac{1}{2}\Delta k \leqslant |\boldsymbol{k}'| < k+\tfrac{1}{2}\Delta k\}, \end{aligned}\right\} \tag{3.2}$$

is analysed. We make use of the fact that the large-k behaviour of $E(k,t)$ is related to the width $\delta(t)$ of the analyticity strip of $\boldsymbol{v}(\boldsymbol{z},t)$ as a function of $\boldsymbol{z}=\boldsymbol{x}+\mathrm{i}\boldsymbol{y}$ ($\boldsymbol{x},\boldsymbol{y}\in\mathbb{R}^3$) which is determined by the singularity of $\boldsymbol{v}(\boldsymbol{z},t)$ with smallest modulus $\min|\mathrm{Im}\,\boldsymbol{z}| = \delta(t)$ (Sulem *et al.* 1983; Frisch 1983). For finite $\delta(t)$, the leading large-k behaviour of $E(k,t)$ is exponential, as

$$\ln E(k,t) \sim -2\delta(t)\,k. \tag{3.3}$$

If, however, at some time t_* the width $\delta = 0$, the flow develops a singularity in real (physical) space, and the leading behaviour of $E(k,t_*)$ is typically a power law:

$$\ln E(k,t_*) \sim -n(t_*)\ln k. \tag{3.4}$$

In the latter case, $\Omega_\lambda(t_*)$ diverges for $\lambda > \frac{1}{2}(n(t_*)-1)$. Thus, in order to study the question of finite-time physical-space singularities in the flow, it is useful to analyse the temporal behaviour of the analyticity-strip width $\delta(t)$ and to determine whether $\delta(t)$ vanishes at some finite time. This method has the great advantage that no actual analytic continuation is required.

We have computed the temporal evolution of the spectrum by numerical integration of the three-dimensional Euler equations with the TG initial condition (1.1) using a full spectral (de-aliased pseudospectral) method (see appendix B). The calculations are done with different spatial resolution corresponding to maximum wavenumber components $k_{\max} = 10, 20, 42$ and 84 (which correspond respectively to 32^3, 64^3, 128^3 and 256^3 spectral computations – see appendix B). This may be compared with the values $k_{\max} = 23$ in the $O(t^{44})$ series calculation (MOF) and $k_{\max} = 41$ discussed in §4.

In figure 3 the spectrum $E(k,t)$ is plotted for various t on a linear–log scale for the inviscid calculation with resolution $k_{\max} = 84$; averages are computed over spherical shells of width $\Delta k = 1$. For early times, $t < 1.5$, the large-k behaviour is clearly exponential. However, in contrast with the results obtained in the two-dimensional magnetohydrodynamic problem (Morf *et al.* 1981), where $\log E(k,t)$ is very close to an exact straight line, in the present case algebraic prefactors are clearly important.

For later times, an unusual difference between the values for even and odd k develops. This seems to be due both to the spectral truncation and to the special symmetry of the Taylor–Green vortex that leads to significant excitation in structures localized near the impermeable walls (which are separated by π). In the following we will always use averages over spherical shells with width $\Delta k = 2$, which eliminates this particular even–odd asymmetry.

In figure 4 we plot the energy spectrum $E(k,t)$, both in linear–log and log–log scales, again using $k_{\max} = 84$. Also shown, as solid lines, are fits to the computed energy spectrum, using the assumed form

$$E(k,t) = A(t)\,k^{-n(t)}\,\mathrm{e}^{-2\delta(t)\,k}, \tag{3.5}$$

These fits are obtained by least-squares fit of $\log E(k,t)$ with parameters $A(t)$, $n(t)$ and $\delta(t)$. By (3.3), $\delta(t)$ should be a measure of the width $\delta(t)$ of the analyticity strip of $\boldsymbol{v}(\boldsymbol{z},t)$.

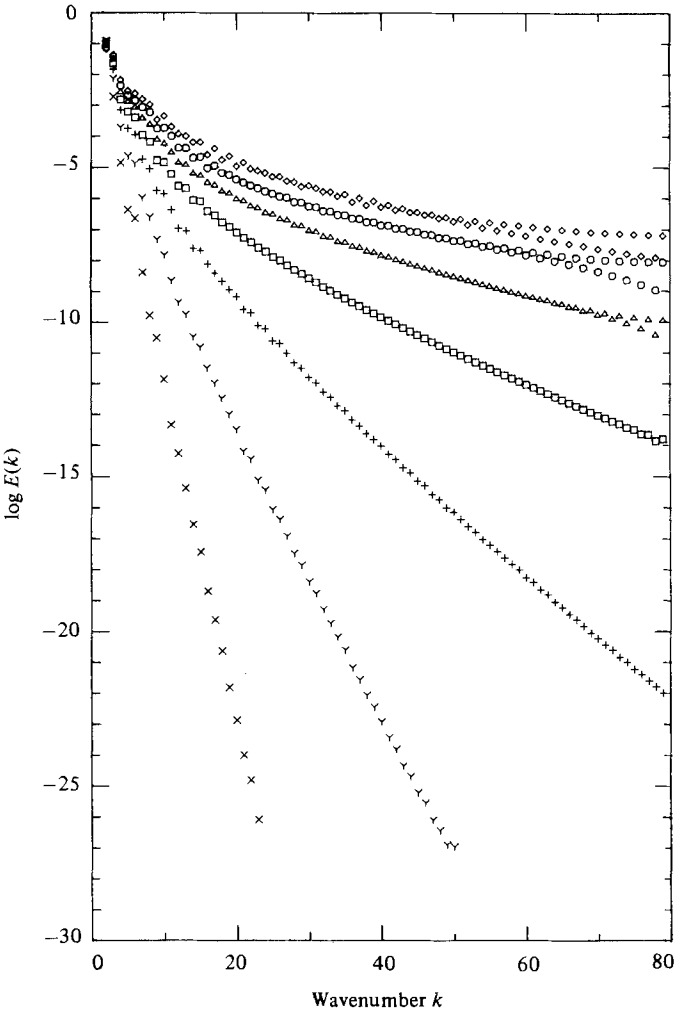

FIGURE 3. The inviscid spectrum $E(k,t)$ defined by (3.2) with $\Delta k = 1$ and resolution $k_{\max} = 84$. The different symbols distinguish the spectra at equally spaced times from crosses at $t = 0.5$ to diamonds at $t = 3.5$ in steps of 0.5.

For early times, the quality of the fit appears to be very good. However, for the two spectra at $t = 3$ and $t = 3.5$, the form (3.5) does not appear to fit the computed spectrum, whose large-k tail appears to decrease more slowly, possibly as the result of spectral truncation.

In table 1, we give the values of $n(t)$ and $\delta(t)$ obtained from these fits. Results from computations with $k_{\max} = 42$ and 84 are listed. For the fits, we use all values of $E(k)$ with $10 \leqslant k \leqslant 36$ for the lower-resolution and $10 \leqslant k \leqslant 75$ for the higher-resolution computations, with the constraint $E(k,t) > 10^{-27}$ (which is the level of roundoff error). For $t = 0.5$, $E(k,t)$ is fitted using $4 \leqslant k \leqslant 22$. The results given in columns 2–5 are obtained from least-squares fits for all three parameters $A(t)$, $n(t)$ and $\delta(t)$. Clearly for early times $t \leqslant 2$ the results for $n(t)$ and $\delta(t)$ do not depend significantly on the resolution. However, for later times the fact that the logarithmic decrement $\delta(t)$ changes sign signals the breakdown of these computations. For the lower-resolution calculation this appears to occur around $t = 2.5$, while the higher-resolution computation appears to remain reliable somewhat longer.

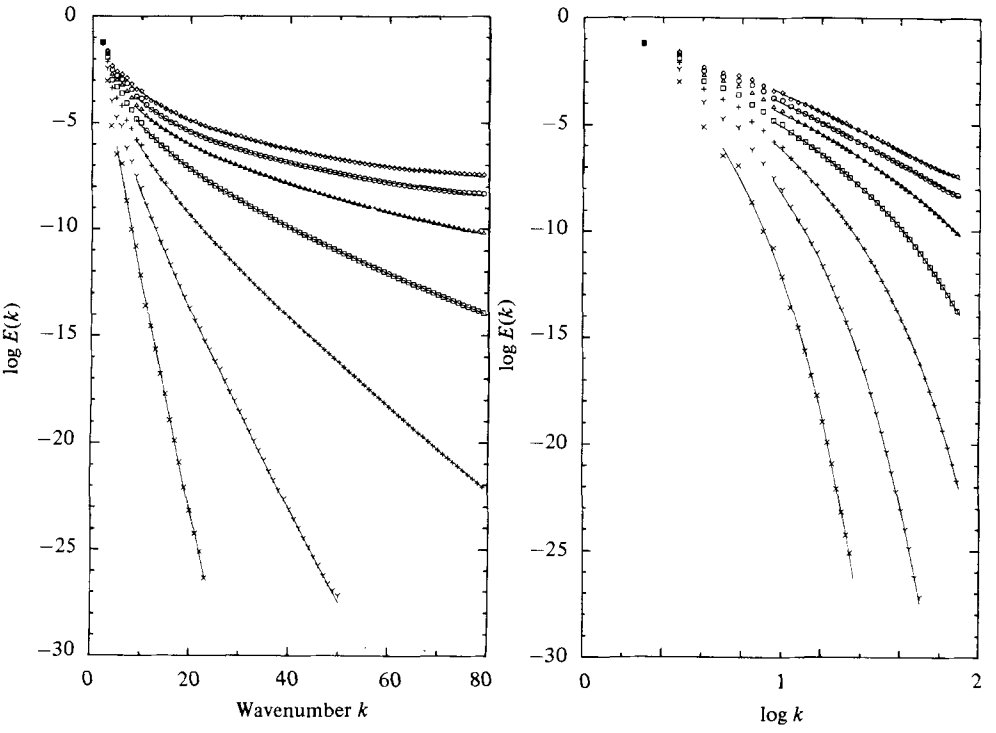

FIGURE 4. The inviscid spectrum $E(k,t)$ as in figure 3 but with $\Delta k = 2$. Solid lines are the fits to (3.5) with the parameters listed in table 1.

We note that the logarithmic decrement at consecutive times has a nearly constant ratio $\delta(t)/\delta(t+0.5) \approx 2.4$, which extends up to a time of $t = 2$ for the lower-resolution and up to $t = 2.5$ for the higher-resolution calculation. From this we may infer that, at times $t \lesssim 2.5$, $\delta(t)$ varies exponentially with time:

$$\delta(t) = \delta_0 \exp(-t/T) \tag{3.6}$$

with a relaxation time $T \approx 0.57$ and $\delta_0 \approx 2.6$ (see figure 5). This corresponds to a doubling of the exponential cutoff wavenumber δ^{-1} in a time interval $\Delta t \approx 0.40$. Of course (3.6) cannot be valid for very short times; some form of non-exponential transient must be present since at $t = 0$ only one mode is excited and hence $\delta(t = 0) = \infty$. Additional consistency checks to determine better the range of validity of the exponential (3.6) are described below.

In table 1 (columns 7 and 8) we also show the values for $n(t)$ that result from a least-squares fit with prescribed values $\delta(t)$, given by (3.6) and tabulated in column 6. The algebraic prefactor is characterized by an exponent $n(t)$ which varies between $5 > n(t) > 4$ and appears to approach 4 for long times. (It is possible that $n(t) \approx 4$ reflects the essentially two-dimensional excitation near the walls of the impermeable cube. Quasi-two-dimensional inviscid dynamics are likely to produce surfaces across which rapid vorticity variations occur, resulting in a k^{-4} spectrum (see Saffman 1971 and §7)). It is interesting to note that, when prescribing $\delta(t)$, the resulting $n(t)$ varies only insignificantly with resolution. Also listed in columns 9 and 10 is the increase $\Delta\sigma/\sigma$ (in per cent) of the standard deviation σ which results from prescribing the value of $\delta(t)$ according to (3.6). As can be seen, at times t at which the computation is reliable, prescribing $\delta(t)$ does not change the standard deviation appreciably. In

	$\delta(t)$, $n(t)$, $A(t)$ fitted				$\delta(t)$ prescribed			$\Delta\sigma/\sigma$ (prescribed)	
	$\delta(t)$		$n(t)$			$n(t)$			
t	42	84	42	84	$\delta(t)$	42	84	42	84
0.5	1.107	1.107	4.31	4.31	1.106	4.35	4.35	0	0
1.0	0.453	0.451	5.02	5.14	0.461	4.68	4.61	2	10
1.5	0.193	0.192	4.79	4.86	0.192	4.85	4.84	0	0
2.0	0.080	0.080	4.48	4.50	0.080	4.48	4.50	0	0
2.5	0.020	0.034	4.71	4.18	0.034	4.13	4.18	65	0
3.0	−0.022	0.005	5.63	4.59	0.014	4.06	3.96	127	162
3.5	−0.007	−0.002	4.51	4.56	0.006	3.94	4.04	23	35

TABLE 1. Three- and two-parameter fit for energy spectrum $E(k, t)$

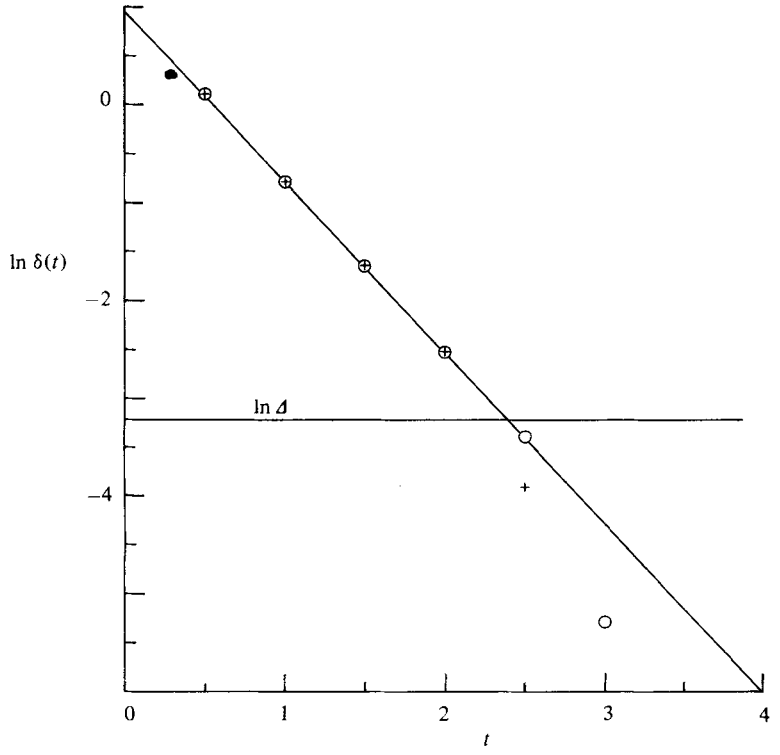

FIGURE 5. The time dependence of the width of the analyticity strip δ in (3.5) from the data of table 1. Circles are based on fits with $k_{\max} = 84$; plus signs are obtained with $k_{\max} = 42$. The horizontal line is the 'effective' resolution $\Delta = \pi/k_{\max} = \frac{1}{84}\pi$ to indicate the expected resolution limit of $\delta(t)$. The solid line is the fit (3.6) to the data.

fact, at early times the relatively large values of $\delta(t)$ do not allow us to separate the exponential and power-law terms accurately (cf. (3.5)).

The latter result may also be seen from the results given in table 2, which show the sensitivity of the least-squares fit to the range of k-values $K_{\min} < k < K_{\max}$ that is used for the fit. Results are from the $k_{\max} = 84$ computation. Clearly, at early times $t \lesssim 1$, the values of $n(t)$ and $\delta(t)$ fluctuate significantly as $K_{\min}$ and $K_{\max}$ are varied. For $1.5 \lesssim t \lesssim 2.5$ both $n(t)$ and $\delta(t)$ appear to be reasonably independent of the range

T	$K_{\min}$	$K_{\max}$	$n(t)$	$\delta(t)$
0.5	9	16	10.80	0.85
	14	22	2.74	1.16
1.0	10	30	4.97	0.46
	24	44	4.12	0.47
1.5	10	40	4.79	0.20
	25	55	5.21	0.19
	40	70	4.04	0.20
2.0	10	40	4.43	0.08
	25	55	4.63	0.08
	40	70	4.34	0.08
2.5	10	40	4.36	0.029
	25	55	3.99	0.036
	40	70	4.09	0.035
3.0	10	40	4.87	−0.001
	25	55	4.11	0.011
	40	70	4.50	0.007
3.5	10	40	3.79	0.014
	25	55	4.75	0.000
	40	70	7.09	−0.026

TABLE 2. Sensitivity of fit to choice of $K_{\min}$ and $K_{\max}$

of k-values used for the fit. It is also in this regime that the exponential law (3.6) is best satisfied.

We conclude that by spectral fitting alone and with the resolution available we cannot confirm the existence of a finite-time singularity in the TG flow. However, to make additional and more direct contact with MOF and §4, we present results for the temporal evolution of the enstrophy $\Omega_1(t)$ and its time derivative $(\mathrm{d}/\mathrm{d}t)\,\Omega_1(t)$ which have been computed for resolutions corresponding to $K \equiv k_{\max} = 10$, 20, 42 and 84. Based on the observed behaviour (3.5) of the spectrum $E(k,t)$ it is also possible to extrapolate these results to infinite resolution ($k_{\max} = \infty$). This has been done using the assumed form

$$F(\infty) = F(K) + bK^{-m}\,\mathrm{e}^{-dK}, \tag{3.7}$$

where $F(K)$ stands for the resolution K-dependent values of $\Omega_1(t)$ or its time derivative. From the four values for $K = 10$, 20, 42, 84, the four parameters b, m, d and $F(\infty)$ can be determined. In tables 3 and 4, we list the values for $\Omega_1(t)$ and $(\mathrm{d}/\mathrm{d}t)\,\Omega_1(t)$ obtained in this way. Beyond $t \approx 3.5$ the latter cannot be extrapolated with confidence. Since our $k_{\max} = 84$ is considerably larger than the corresponding $k_{\max} = 23$ of MOF, their claim that an extrapolation to $t \approx 5$ is possible is not supported by the present results. Indeed, a more realistic estimate of the maximum t that can be reached by the series method will be given in §4.

In addition, we are now also in a position to estimate, *a posteriori*, the maximum time $\bar{t}$ for which our solution of the Euler equations for the TG flow should be correct in complete detail. Clearly we expect inaccuracies in the numerical results whenever $\delta(t) \lesssim \Delta$, where Δ is the effective grid resolution given by $\Delta = \pi/k_{\max}$. If we use (3.6) as an approximation to the true δ and set $\delta(\bar{t}) = \Delta$, we obtain $\bar{t} = 2.0$ for $k_{\max} = 42$ and $\bar{t} = 2.4$ for $k_{\max} = 84$ (see figure 5). If we use the more optimistic condition $\delta(\bar{t}) = \frac{1}{2}\Delta$, each $\bar{t}$ is increased by 0.4. In either case, our spectral fits are completely consistent with the assumption that (3.6) is valid for all times greater than 1.5; however, we cannot exclude the possibility that a crossover in the behaviour of the

t	10	20	42	84	∞
0	0.37500	0.37500	0.37500	0.37500	0.37500
0.25	0.37745	0.37746	0.37746	0.37746	0.37746
0.5	0.38495	0.38495	0.38495	0.38495	0.38495
0.75	0.39789	0.39789	0.39789	0.39789	0.39789
1	0.41691	0.41691	0.41691	0.41691	0.41691
1.25	0.44287	0.44288	0.44288	0.44288	0.44288
1.5	0.47684	0.47686	0.47686	0.47686	0.47686
1.75	0.52001	0.52016	0.52016	0.52016	0.52016
2	0.57360	0.57433	0.57435	0.57435	0.57435
2.25	0.63866	0.64114	0.64129	0.64130	0.64130
2.5	0.71616	0.72254	0.72329	0.72333	0.72333
2.75	0.80731	0.82070	0.82317	0.82345	0.82347
3	0.91425	0.93866	0.94474	0.94593	0.94608
3.25	1.04036	1.08190	1.09436	1.09782	1.09875
3.5	1.18988	1.26142	1.28671	1.29452	1.29652
3.75	1.36429	1.49774	1.55829	1.57908	1.58307
4	1.57009	1.82328	1.97494	2.06562	2.15798

TABLE 3. Extrapolation of $\Omega_1(t)$ to infinite resolution

t	10	20	42	84	∞
0	0.00000	0.00000	0.00000	0.00000	0.00000
0.25	0.01972	0.01972	0.01972	0.01972	0.01972
0.5	0.04052	0.04052	0.04052	0.04052	0.04052
0.75	0.06342	0.06342	0.06342	0.06342	0.06342
1	0.08933	0.08933	0.08933	0.08933	0.08933
1.25	0.11909	0.11911	0.11911	0.11911	0.11911
1.5	0.15344	0.15362	0.15362	0.15362	0.15362
1.75	0.19274	0.19381	0.19383	0.19383	0.19383
2	0.23667	0.24070	0.24089	0.24089	0.24089
2.25	0.28448	0.29507	0.29619	0.29623	0.29623
2.5	0.33626	0.35752	0.36161	0.36198	0.36199
2.75	0.39432	0.42968	0.43984	0.44173	0.44187
3	0.46352	0.51740	0.53656	0.54245	0.54386
3.25	0.54791	0.63550	0.66919	0.68175	0.68758
3.5	0.64577	0.81410	0.89282	0.91714	0.92033
3.75	0.75680	1.09784	1.32526	1.43250	?
4	0.89657	1.53513	2.05686	2.59199	?

TABLE 4. Extrapolation of $(\mathrm{d}/\mathrm{d}t)\,\Omega_1(t)$ to infinite resolution

flow might occur at a time $t \gtrsim 3$. In fact, we believe we have good indirect evidence that such a crossover does occur.

The indirect evidence is predicated by our assumption that spatially and temporally slowly varying quantities are not dramatically affected by errors in high-wavenumber structure. For example, the strain rate or convergence $-\nabla\cdot\boldsymbol{v}$ at $x = z = \frac{1}{2}\pi$, $y = 0$ is determined primarily by the inertia in the large-scale eddies and not by the rapidly growing vorticity in the sheet structure near this point. The numerical values $-\nabla\cdot\boldsymbol{v} = 0.53$, 1.09, and 4.17 for times $t = 2$, 3 and 4 respectively, as shown in figures 1 and 2, are accurate to a few per cent, based on comparing the results of $(128)^3$ and $(256)^3$ runs. A further reasonable assumption, which is confirmed by the model

calculation of appendix D, is that we can equate the fractional rate of increase of the vorticity with the fractional rate of decrease of the analyticity-strip width $\hat{\delta}$. That is,

$$\nabla \cdot \boldsymbol{v}_{\parallel} \approx \frac{\mathrm{d}}{\mathrm{d}t} \ln \hat{\delta}. \tag{3.8}$$

We can thus 'derive' the exponential form (3.6) with a relaxation time $T \approx |\nabla \cdot \boldsymbol{v}_{\parallel}|^{-1}$ that is weakly dependent on time. Given our numerical results for $\nabla \cdot \boldsymbol{v}_{\parallel}$ we obtain $T = 1.89$, 0.92 and 0.24 for $t = 2$, 3 and 4. This corresponds to a doubling of the exponential cutoff wavenumber $\hat{\delta}^{-1}$ due to this particular flow structure in time intervals $\Delta t = 1.3$, 0.6, and 0.2 This result should be compared with the estimate $\Delta t = 0.40$ obtained by fitting the spectrum of the complete flow field.

In the evolving TG flow, there are several disconnected regions displaying small-scale activity. Each one is likely to be associated with nearby complex-space singularities whose distance $\hat{\delta}(t)$ from physical space has its own time dependence. At each time, the region with the smallest $\hat{\delta}(t)$ dominates the asymptotically high-wavenumber spectrum, but the $\delta(t)$ obtained by spectral fitting using (3.5) may reflect the influence of various regions yielding overlapping contributions in k-space. In particular, the result (3.6) for $\delta(t)$ with $1.5 \lesssim t \lesssim 2.5$ cannot reflect the influence of the high-strain-rate region near $x = z = \frac{1}{2}\pi$, $y = 0$ for $t > 3.5$ if the above discussion of (3.8) is realistic.

In summary, the inviscid time-dependent computations reported here show the early-time spectrum is well fitted by (3.5), that the exponential decrement $\delta(t)$ satisfies (3.6), and that the algebraic prefactor $n(t)$ decreases slowly towards 4 as t increases. However, we have indirect evidence that a more rapid decay of δ must occur for $t > 3.5$. Finally, our resolution is not adequate to investigate the possibility of a real-time singularity in the flow for $t \gtrsim 4$.

4. Analysis of the inviscid flow: power-series results

With analytic initial data, the solution of the Euler equations for three-dimensional inviscid, incompressible flow has, at short times, a convergent power-series solution (Frisch 1983 and references therein)

$$\boldsymbol{v}(\boldsymbol{r}, t) = \sum_{p=0}^{\infty} t^p \boldsymbol{v}^{(p)}(\boldsymbol{r}) \tag{4.1}$$

The $\boldsymbol{v}^{(p)}$ can be obtained by recursion:

$$p \sum_j \frac{\partial}{\partial r_j} \frac{\partial}{\partial r_j} v_i^{(p)} = \sum_{j,k} \frac{\partial}{\partial r_j} \frac{\partial}{\partial r_k} \left(\frac{\partial}{\partial r_i} s_{jk}^{(p)} - \frac{\partial}{\partial r_j} s_{ik}^{(p)} \right), \tag{4.2}$$

where $\boldsymbol{r} = (x, y, z)$ and

$$s_{ij}^{(p)} = \sum_{q=0}^{p-1} v_i^{(q)} v_j^{(p-q-1)}. \tag{4.3}$$

Equation (4.2) is derived by substituting (4.1) into the Euler equations for $(\partial/\partial t)(\nabla \times (\nabla \times \boldsymbol{v}))$. For the TG initial conditions (1.1) the modal decomposition (1.2) holds with the important simplification that $u_i^{(q)}(m, n, p)$ is identically zero whenever m, n, or $p > q+1$. Here we choose $\theta = 0$ in (1.1). Because of the even/odd decomposition of (1.2), the power-series coefficients $\boldsymbol{v}^{(p)}(\boldsymbol{r})$ can always be deduced for all $\boldsymbol{r}$ in the periodicity box from their values in the fundamental box $0 \leqslant x, y, z \leqslant \frac{1}{2}\pi$ alone. Furthermore, if we specify $v_i^{(p)}$ at N^3 uniformly spaced points in this fundamental box, the M^3 mode coefficients $u_i^{(P)}$ with $M = [\frac{1}{2}(P+3)]$ can be obtained exactly provided that $P \leqslant 2N-2$. For $2N-2 < P \leqslant 4N-3$, the lowest M^3 modes

$u_i^{(P)}(m,n,p)$ with $M = 2N-1-[\frac{1}{2}P]$ will still be given correctly, although the higher-order coefficients in which any of m, n, or p is greater than or equal to M are in error because of aliasing. However, aliasing is not a disadvantage for the calculation of the generalized enstrophy series (3.1). Indeed, the coefficients $A_\lambda^{(2r)}$ involve velocity modes only in the form of products $\boldsymbol{u}^{(q)}(m,n,p)\cdot\boldsymbol{u}^{(2r-q)}(m,n,p)$ so they will be given correctly for $r \leqslant 2N-2$. It is the realization of this very specific control on the effects of aliasing in the transform solution of the TG vortex that enables the present extension of the results of MOF.

The outline of the new series solution is as follows. To generate the coefficients of t^p in the expansion of v_x and v_z, we evaluate the four independent sums of products $s_{xx}^{(p)}$, $s_{xy}^{(p)}$, $s_{xz}^{(p)}$ and $s_{zz}^{(p)}$ at N^3 points in coordinate space. Four Fourier transforms convert these sums to momentum space, and the M^3 mode coefficients for each sum are then multiplied by the appropriate combination of momenta to yield the M^3 contributions to $u_x^{(p)}$ and $u_z^{(p)}$. Two more Fourier transforms yield $v_x^{(p)}$ and $v_z^{(p)}$ back in coordinate space, and thus complete the order-t^p calculation.

The time for the entire calculation is dominated by the multiple-precision multiply operations as counted below. The four coordinate-space sums of products require $4N^3p$ multiplies at order t^p or $4N^3\sum_{p=0}^{4N-4} p \approx 32N^5-56N^4$ operations in total. The six Fourier transforms at order t^p require $6(NM^3+N^2M^2+N^3M)$ multiply operations, where M is the minimum of $[\frac{1}{2}(p+3]$ and $2N-1-[\frac{1}{2}p]$. In total, this is

$$6\sum_{p=0}^{4N-4}(NM^3+N^2M^2+N^3M) \approx 26N^5+18N^4.$$

Finally, there are about $16M^3$ multiple-precision momentum multiplications (computation of $\boldsymbol{r}$-derivatives of $s^{(p)}$) on the mode coefficients at order t^p, or about

$$16\sum_{p=0}^{4N-4} M^3 \approx 16N^4$$

in total. If we ignore the small additional effort in the step of determining the generalized enstrophy, we obtain a final multiply count of nearly $58N^5$. For the present $N = 21$ or order-t^{80} calculation this is roughly 2.4×10^8 and required just under one hour of CPU time on the University of Guelph Amdahl V/5 computer with the available IBM Fortran quadruple precision (28 hexadecimal) facility. Note that, since the dominant multiplications occur naturally in vector form, considerable extension of the present series should be possible with the use of array processors (assuming the availability of efficient extended-precision utilities).

The enstrophy expansion coefficients $A_\lambda^{(2r)}$ are given in table 5 for $\lambda = 1$ and 2. The number of significant digits was estimated by comparing runs with $N = 19$ *vs.* $N = 21$. The loss of significance appears to be one half-decade with each other in t^2, and the computer output in table 5 has been truncated at this rate. We believe each entry is significant except for the last two or three digits.

We have concentrated our analysis on $\Omega_1(t)$, which appears to be the most tractable of the series for Ω_λ, $\lambda = 1,\ldots,4$. Padé, Dlog Padé (Baker 1975), and first-order inhomogeneous differential approximants (Fisher & Au-Yang 1979, 1980; Hunter & Baker 1979) suggest singularities at $t^2 = -4.65\pm0.05$ and at $t^2 = (1.5\pm0.2)\pm(5.4\pm0.2)\,\mathrm{i}$. An additional singularity appears to be present at $|t^2| \approx 15$–20 either on the positive real axis or as a nearby complex-conjugate pair.

The uncertainty in the nature of this latter singularity is well illustrated in table 6, in which we give a partial list of Padé approximants of Ω_1 together with *all* their

r	$\lambda = 1$	$\lambda = 2$
0	0.75000000000000000000000000000E+00	0.22500000000000000000000000000E+01
1	0.78124999999999999999999999995E−01	0.85937499999999999999999999995E+00
2	0.59185606060606060606060606601E−02	0.18353456439393939393939393992E+00
3	−0.27843606425347977381470204436711E−03	0.17807023207554008989415687980277E−01
4	0.61048213608414040976589547497500E−04	0.35451738847569529320279397090410E−02
5	−0.96361343406379096996080171679830E−05	0.10098906502725140420865976260550E−03
6	0.12376451432939409337723444617600E−05	0.38823461957491314314096971518500E−04
7	−0.13001673399485842050532230751800E−06	0.22368045027131653384316208347200E−05
8	0.11507664940214605511186628852000E−07	−0.72755266671209462846336491413000E−06
9	−0.40689927930502918781244653498000E−09	0.30029547904711509299480585942000E−06
10	−0.15722647048717447228204712700000E−09	−0.83009469407294339014946906690000E−07
11	0.56457081462142300009592373250000E−10	0.20213823695562241637115660190000E−07
12	−0.13696928782856063280154415300000E−10	−0.45936905982240854370304080000E−08
13	0.29920198954228640442791535000000E−11	0.10081979947369894739120989200000E−08
14	−0.61991963183363252307722688000000E−12	−0.21405544207569641023147544000000E−09
15	0.12450945726913139691007882000000E−12	0.44376078120715792074723467000000E−10
16	−0.24774479828999593771452870000000E−13	−0.90809463860353078123658570000000E−11
17	0.49252841340330883023774810000000E−14	0.18378634138382275010501900000000E−11
18	−0.97719041829306565745462900000000E−15	−0.36824652690299825990970400000000E−12
19	0.19375444767106104429043700000000E−15	0.73343554096933041294280100000000E−13
20	−0.38505990845347852748213000000000E−16	−0.14552051190124197113072000000000E−13
21	0.76701287226861612998270000000000E−17	0.28765653657163787739286000000000E−14
22	−0.15301069631879348281350000000000E−17	−0.56722619641517073577980000000000E−15
23	0.30585009158637265652730000000000E−18	0.11175469555996388194050000000000E−15
24	−0.61279386047170433163800000000000E−19	−0.22007500306260941504600000000000E−16
25	0.12302069798992531554700000000000E−19	0.43331789639558287640600000000000E−17
26	−0.24743842723469146812000000000000E−20	−0.85378166839805092519000000000000E−18
27	0.49871740662854581144000000000000E−21	0.16842136033860529072000000000000E−18
28	−0.10071233331935838450000000000000E−21	−0.33265082711349649070000000000000E−19
29	0.20373933972348344470000000000000E−22	0.65804799172009642690000000000000E−20
30	−0.41289304714858419800000000000000E−23	−0.13042140830438503500000000000000E−20
31	0.83820874296160258400000000000000E−24	0.25898530649691768400000000000000E−21
32	−0.17043406330511116000000000000000E−24	−0.51528418224404805000000000000000E−22
33	0.34707362620876885000000000000000E−25	0.10273619100869626000000000000000E−22
34	−0.70784176151137040000000000000000E−26	−0.20526365443944830000000000000000E−23
35	0.14456490670569290000000000000000E−26	0.41094124984181460000000000000000E−24
36	−0.29564188944707500000000000000000E−27	−0.82437341799265700000000000000000E−25
37	0.60538014508785700000000000000000E−28	0.16570716814015100000000000000000E−25
38	−0.12411584017048000000000000000000E−28	−0.33373074534565000000000000000000E−26
39	0.25476148544746000000000000000000E−29	0.67337724703878000000000000000000E−27
40	−0.52351228744960000000000000000000E−30	−0.13611693391260000000000000000000E−27

TABLE 5. Coefficients $A_\lambda^{(2r)}$ in the expansion (3.1) of $\Omega_\lambda(t)$

Approximant	Complex-t^2 plane pole locations with ($\|\arg t^2\| < \frac{1}{4}\pi$)		$\left.\frac{d\Omega_1}{dt}\right\|_{t=4}$
[17/22]	18.94,	$16.58 \pm 11.33i$	3.98
[18/21]	20.53,	$15.84 \pm 7.89i$	3.16
[19/20]	31.32,	$15.65 \pm 4.43i$	2.03
[20/19]	31.12,	$15.66 \pm 4.45i$	2.04
[21/18]	—	$14.94 \pm 3.19i$	1.23
[19/22]	20.05,	$15.66 \pm 8.54i$	3.32
[19/21]	19.95,	$15.56 \pm 8.64i$	3.35
[21/19]	18.50,	$14.29 \pm 7.35i$	3.91
[22/18]	—	$15.76 \pm 4.05i$	1.87

TABLE 6. Singularities and estimates of Ω_1 from Padé approximants

pole locations with $|\arg t^2| < \frac{1}{4}\pi$. Since in most cases the poles shown in table 6 are also the poles furthest from the t^2 plane origin, their almost 'random' position is not that surprising. We believe that this 'randomness' is attributable to lack of information, i.e. the limited number of series coefficients available, rather than to roundoff error in the known series coefficients. This conclusion is based on our observation that approximants determined from 40 terms of the series typically predict the last, i.e. the 41st, term to 7-figure accuracy; we believe this coefficient has 3 more significant digits.

Our lack of understanding of the unphysical singularities of Ω_1 seriously hampers our attempts to deduce its analytic structure for real times. For example Padé approximants represent Ω_1 near the negative real $-t^2$ axis by a string of poles. The [21/19] approximant is typical, with pole locations at $t^2 = -4.75$, -5.05, -5.59 and -7.75, suggesting that $t^2 \approx -4.7$ is a branch-point singularity. However, Dlog Padé approximants show similar structure (the typical approximant [21/18] has poles (residues) at $t^2 = -4.69(0.02)$, $-4.91(0.03)$, and $-6.25(-0.12)$), so that a simple branch-point interpretation is not correct. Finally, inhomogeneous approximants suggest that a branch point with analytic background is not correct either. We can certainly not exclude the very complicated confluent-type behaviour and natural boundary structure discussed by Chang *et al.* (1982) for a much simpler Hamiltonian system. In fact, such behaviour would explain our observation that all these analysis methods yield comparable results.

In figure 6 we plot estimates of $d\ln\Omega_\lambda(t)/d(t^2)$ given by various approximants. Notice that there is a divergence in the estimates for $\lambda = 1$ beyond $t^2 \approx 13$. Approximants based on the series limited to order t^{44} show divergence beyond $t^2 \approx 11$. This latter divergence is not apparent in the diagonal Padé sequence studied by MOF; we believe the present results based on both diagonal *and* near-diagonal Padé estimates give a more realistic view of the convergence of the method. Also, the numerical estimate of the maximum times $t \approx \sqrt{11} = 3.3$ and $t \approx \sqrt{13} = 3.6$ for which MOF and the present calculations for Ω_1 are reliable show that for spatially averaged quantities there is no particular advantage in series methods compared to direct simulation. The same loss of resolution appears to limit both calculations. Similar conclusions can be drawn from estimates of the generalized enstrophies Ω_λ, with the additional results that the believable t-range is more restricted for $\lambda > 1$.

The results of the present series analysis of Ω_λ are consistent with the time-integration results presented in §3, at least for $t \lesssim 2.5$. In particular, the present results

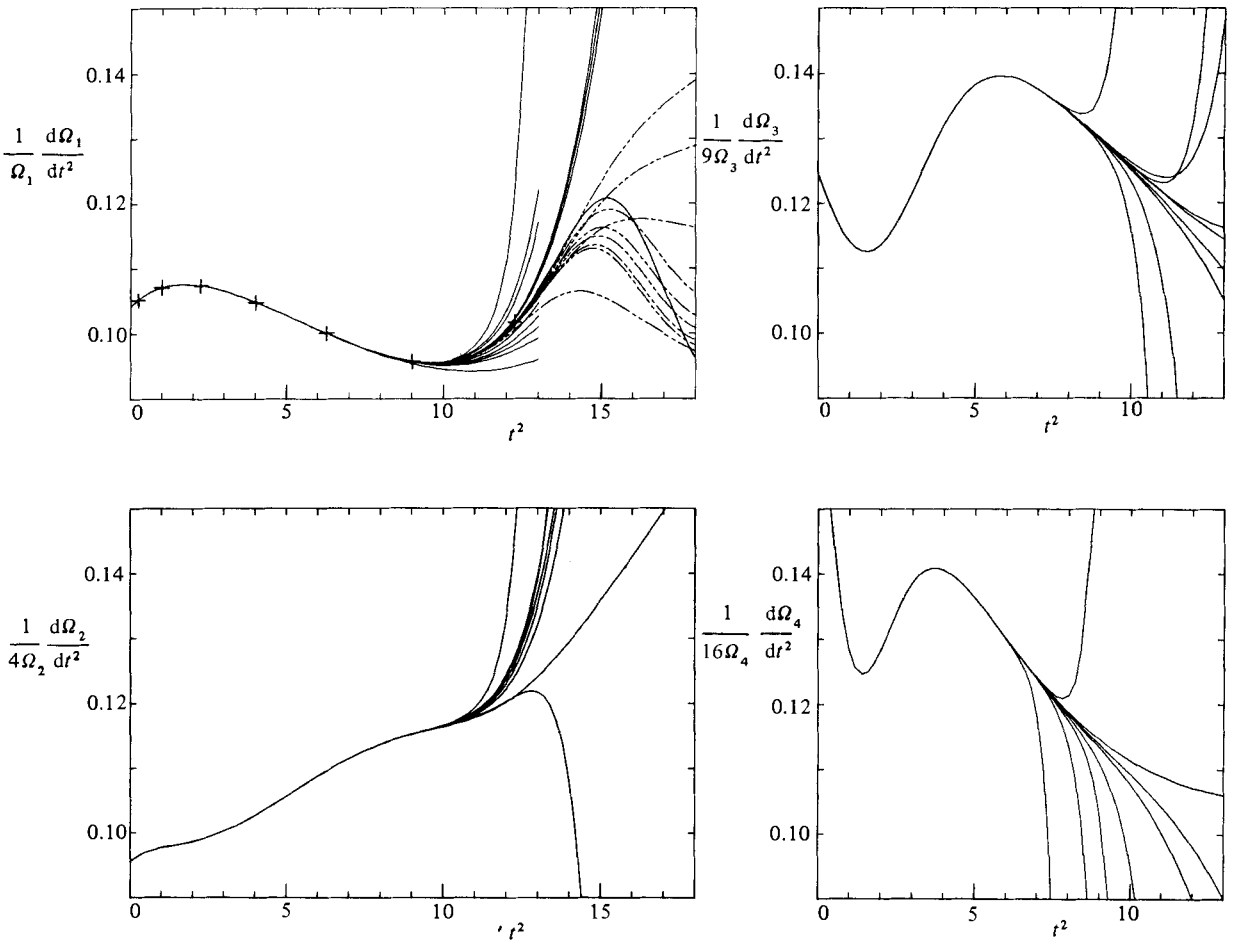

FIGURE 6. Near-diagonal Padé and Dlog Padé approximants for the generalized enstrophies $d \ln \Omega_\lambda / d(t^2)$ defined in (3.1). For $\lambda > 1$, all curves are based on the full t^{80} series presented in table 5. For $\lambda = 1$, curves truncated at $t^2 = 13$ are based on the t^{44} series of MOF; the remaining curves use the full t^{80} series. The dashed curves for $\lambda = 1$ are based on Padé and Dlog Padé approximants obtained after a conformal mapping is used to bring the positive real axis closer to the origin relative to the dominant unphysical singularities. No *a priori* preference can be given for the dashed *vs.* solid lines; the differences are an indication of the accuracy of all the approximants. The large crosses for $\lambda = 1$ are the extrapolated estimates given in tables 3 and 4 obtained from the direct-simulation results.

for Ω_4/Ω_3 satisfactorily test the estimates of $n(t)$ and $\delta(t)$ given in tables 1 and 2. Also, as shown in figure 6(*a*), the time-integration results for $(d/d(t^2)) \ln \Omega_1$ are consistent with the series results for $t \lesssim 3.5$.

Finally, for times $t \gtrsim 3.5$ we can usefully combine the series results and direct-simulation studies to gain information which would not be credible when based on either method alone. In particular, the Padé estimates of $(d/dt)\Omega_1$ at $t = 4$ shown in table 6 show such a wide variation as to be virtually useless. Similarly, the direct-simulation estimates of $(d/dt)\Omega_1$ at $t = 4$ shown in table 4 could not be extrapolated with any confidence. However, if, as is reasonable to assume, the estimates of $(d/dt)\Omega_1$ will continue to increase with increasing resolution, then we can conclude that only those Padé approximants that diverge at $t^2 \approx 18$–20 are reasonable. This is the strongest evidence we have at present for a real-time

singularity and its possible time of occurrence $t_* = 4.4 \pm 0.2$. Although the above argument is by no means definitive, it does serve as an excellent example of the complementary nature of the time-series and time-marching techniques used here.

In summary, just as for the direct simulations discussed in §3, the Taylor-series method discussed here does not allow us to say with certainty whether a singularity develops at a time near 4 or, equivalently, whether vorticity can be stretched an infinite amount in a finite time. However, that both methods give consistent results even for such a sensitive quantity as $\mathrm{d}\Omega_1/\mathrm{d}t$ has been useful and we believe that extension of both methods to higher resolution should be explored since each has its relative merits. If the gross features of the flow that have been established by a time of 3 remain unchanged except for the development of a localized singularity, then the idea of extrapolating either local or average properties from exact Taylor coefficients is sound. Although we have not been successful in confirming MOF, somewhat longer series and/or more sophisticated methods of analysis such as, for example, those discussed by Baumel, Gammel & Nuttall (1981) might still work and be more efficient than direct simulation and also avoid the uncontrolled accumulation of errors due to modal truncation. On the other hand, if the flow develops into an infinite cascade of ever smaller vortices, the analytic structure of, say, $\Omega_1(t)$ must be very complicated, and no method of extrapolation from a finite number of Taylor coefficients will ever work. Such a possibility is suggested by our observation that Padé approximants based on 40 terms in the series predict the 41st term to only 7-figure accuracy, implying considerable new information in this last coefficient not obtainable from the preceding terms (increasingly so as the order of the predicted term increases). Thus direct-simulation studies that allow for a visualization of the flow field might be the more useful technique.

5. High-Reynolds-number behaviour

Here we report results obtained by numerical solution of the viscous Navier–Stokes equations for the TG vortex flow. The Reynolds number is $R = 1/\nu$, noting that the length and velocity scales of the initial flow (1.1) are order 1. While the inviscid runs cannot be extended accurately beyond $t \approx 3$, finite-R runs may be accurate for all time. As discussed in appendix B, a $256 \times 256 \times 256$ ($k_{\max} = 84$) run is accurate for all but the smallest dissipation scales provided that $R \lesssim 3000$.

The time evolution of total dissipation $\epsilon(t) = 2\Omega_1(t)/R$ is plotted *vs.* t in figure 7 for $100 \leqslant R \leqslant 3000$. The observed enhancement of mean-square vorticity $\Omega_1(t)$ for small times measures the strength of the nonlinear vortex stretching while the late-time decay of $\epsilon(t)$ reflects the overall decay of the flow by viscous damping.

The results plotted in figure 7 show that the maximum enstrophy $\Omega_{\max}$ is roughly proportional to R as R increases, since the corresponding maximum dissipation varies only weakly with R. The time $t_{\max}$ at which the maximum of dissipation is achieved has been previously observed to be approximately constant in the range $100 \leqslant R \leqslant 400$ (Orszag 1974). Our new results indicate that a secondary maximum appears when $R \gtrsim 500$, leading to a shift in $t_{\max}$ from roughly 7 to roughly 9. We have no evidence for further increase of $t_{\max}$ as R increases, but, of course, this possibility cannot be excluded on the basis of our data.

The small-scale structure of the TG flow undergoes a profound change when $R \gtrsim 500$. A more sensitive measure of this change than the enstrophy is given by the behaviour of the velocity spectral tensor

$$U_{\alpha\beta}(\boldsymbol{k}) = \langle u_\alpha(\boldsymbol{k})\, u_\beta(-\boldsymbol{k}) \rangle,$$

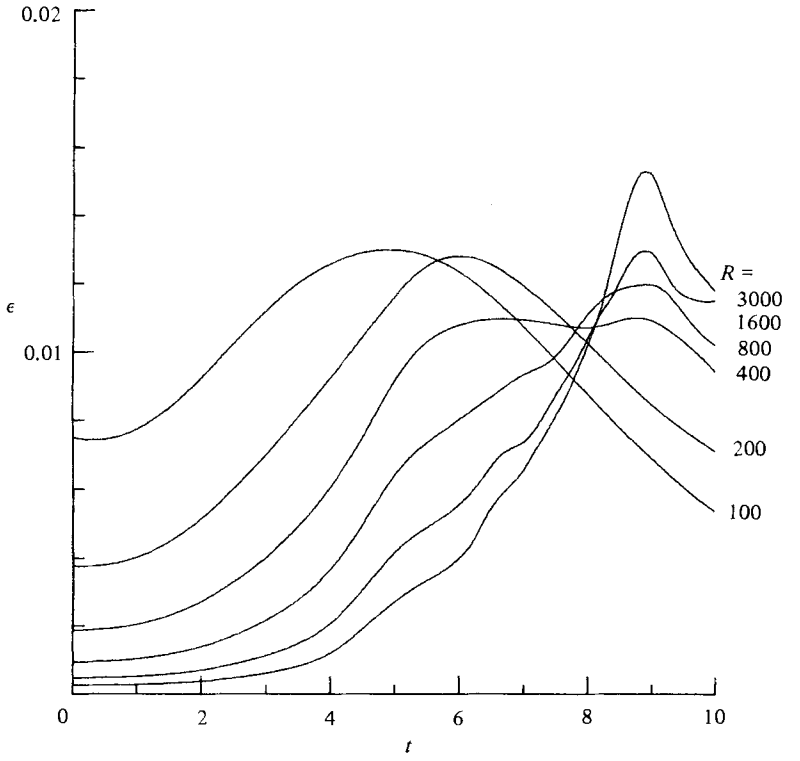

FIGURE 7. Rate of energy dissipation $\epsilon(t)$ ($= 2\nu\Omega_1(t)$) *vs.* t for $100 \leqslant R \leqslant 3000$. Note that the time $t_{\max}$ of maximum dissipation is shifted from $t_{\max} \approx 7$ for $R = 200$ to $t_{\max} \approx 9$ at $R = 3000$.

where $\langle\ \rangle$ indicates an average over the fluctuations of $\boldsymbol{u}$ at wavenumber $\boldsymbol{k}$. In isotropic turbulence, $U_{\alpha\beta}(\boldsymbol{k})$ has the form (cf. Orszag 1977)

$$U_{\alpha\beta}(\boldsymbol{k}) = \frac{E(k)}{4\pi k^2}\left(\delta_{\alpha\beta} - \frac{k_\alpha k_\beta}{k^2}\right), \tag{5.1}$$

where $E(k)$ is the isotropic energy spectrum. One of the basic tenets of the statistical theory of turbulence is that, at sufficiently large R, $U_{\alpha\beta}(\boldsymbol{k})$ should become increasingly isotropic as k increases.

The tendency towards statistical isotropy can be tested by plotting contours of

$$I_{\alpha\beta}(\boldsymbol{k}) = \frac{U_{\alpha\beta}(\boldsymbol{k})}{\delta_{\alpha\beta} - k_\alpha k_\beta/k^2}; \tag{5.2}$$

if isotropy holds, then $I_{\alpha\beta}(\boldsymbol{k})$ is a function of k alone, so its contours for fixed k_y should be circles in the (k_x, k_z)-plane. Here $U_{\alpha\beta}(\boldsymbol{k})$ is calculated by averaging $u_\alpha(\boldsymbol{k})\, u_\beta(-\boldsymbol{k})$ over cubes of side $[\frac{1}{10}k_{\max}]$ centred at $\boldsymbol{k}$ in $\boldsymbol{k}$-space. In figure 8, we plot contours of $I_{11}(\boldsymbol{k})$ and $I_{33}(\boldsymbol{k})$ determined in this way for $R = 400$ and 3000 at $t = 3$, 7, 9 with $k_y = \frac{1}{4}k_{\max}$. It is apparent that both u_x and u_z have significant anisotropies at $t = 3$ at both values of R. At this early time, nonlinear interactions do not have time to overcome the strong anisotropy of the initial conditions (1.1). At $t = 7$ the flow is nearly isotropic for moderately large k when $R = 3000$, but there are still significant anisotropies at large k; at $R = 400$ only u_x has isotropized at $t = 7$. Apparently the local maximum of $\Omega_1(t)$ for $t \approx 7$ for $R \lesssim 400$ is a false indication of the maturity of this flow. On the other hand, it is apparent from figure 8(f) that the flow at $R = 3000$

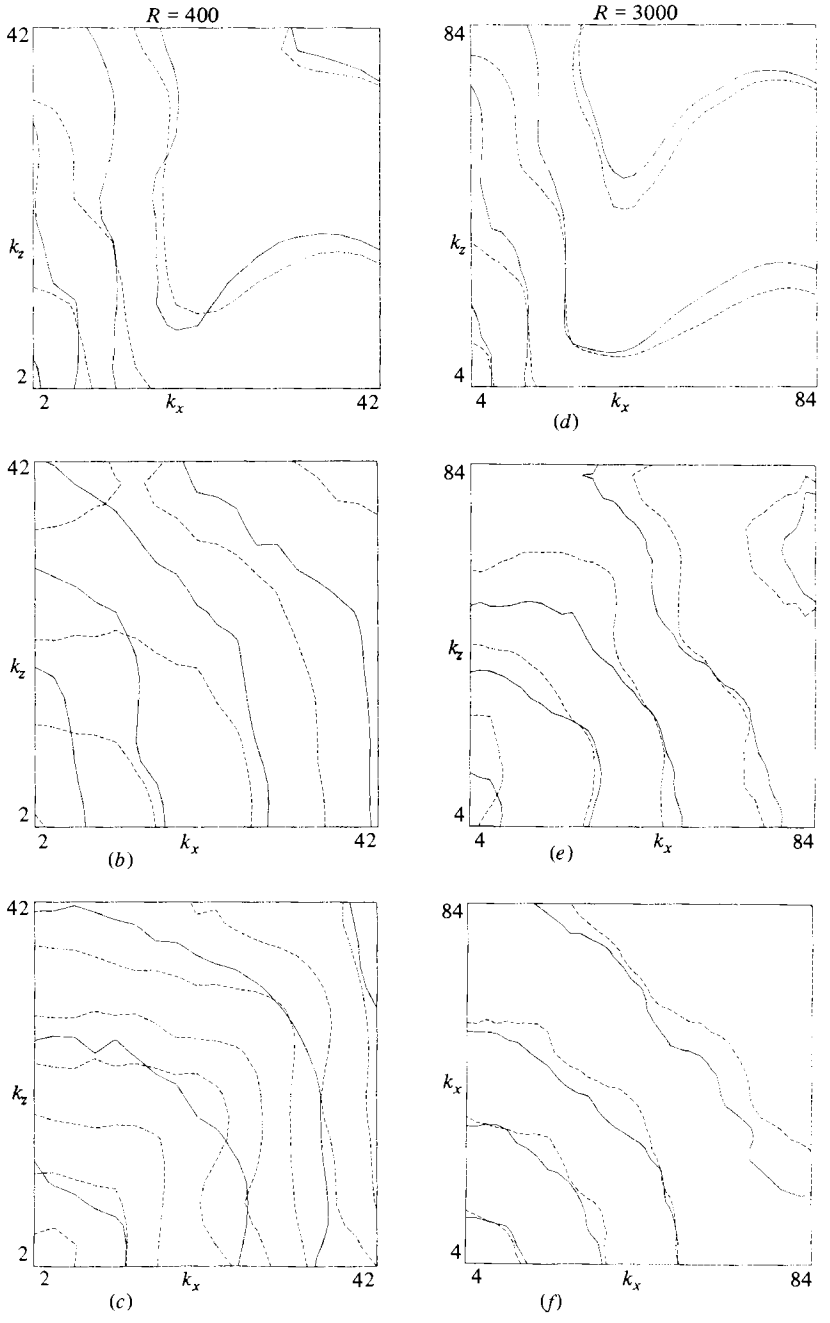

FIGURE 8. Contour plots of $I_{11}(\boldsymbol{k})$ (dashed) and $I_{33}(\boldsymbol{k})$ given by (5.2) for $R = 400$ at $t = 3$ (*a*), 7 (*b*), 9 (*c*) and $R = 3000$ at $t = 3$ (*d*), 7 (*e*), 9 (*f*).

at $t = 9$ is nearly isotropic at large k. In contrast, the flow at $R = 400$ retains some anisotropy (for all t). The result that the flow is isotropic for $t \approx t_{\max}$ at $R = 3000$ is consistent with the results to be reported below on the inertial-range behaviour of the TG flow for $R > 1000$.

Next we analyse spectra of the TG flow at $R = 1600$ and 3000. Isotropic spectra are computed by summing over shells in Fourier space; the energy spectrum $E(k)$ is

Reynolds number	Fit internal	Time 6.8 n	6.8 β	7.8 n	7.8 β	8.8 n	8.8 β	9.8 n	9.8 β
1600	$10 < k < 80$	3.29	0.0091	2.84	0.024	1.47	0.049	1.86	0.043
1600	$13 < k < 83$	3.22	0.0108	3.00	0.020	1.59	0.045	1.98	0.039
3000	$10 < k < 80$	3.20	−0.0019	2.71	0.003	1.73	0.012	2.03	0.009
3000	$13 < k < 83$	3.14	−0.0062	2.68	0.003	1.72	0.012	2.02	0.009

TABLE 7. Least-square fits to the energy spectrum

given by (3.2) with $\Delta k = 1$, no oscillations being observed in these viscous runs at high k when using this narrow-band averaging.

For $t \lesssim 3$, there is good agreement between the high-R viscous runs and the inviscid runs discussed in §3. At these early times, as R increases for fixed k, it appears that the spectrum approaches the spectrum of the inviscid flow. In particular, $E(k)$ behaves exponentially with k as in (2.3), with $\delta(t)$ close to the values given in table 1.

At later times, the high-R runs lead to nearly isotropic high-wavenumber spectra (cf. figure 8) in which the effect of the initial conditions (1.1) is largely forgotten. However, because of the limited Reynolds number of the runs, inertial and dissipation ranges have considerable overlap; it is not possible to run at considerably higher R because of the limited spatial resolution of our code. In order to extract information for such quantities as power-law exponents or dissipative wavenumber cutoffs, we have resorted to analysing the data in terms of an assumed functional form of $E(k)$ for moderate-to-large k. As in §7 we fit $\log E(k)$ by a function of the form

$$E(k,t) = A(t)\,\mathrm{e}^{-\beta(t)\,k}\,k^{-n(t)}. \tag{5.3}$$

By fitting $E(k)$ in this way, we can separate inertial and dissipation range behaviour; the form (5.3) allows a good fit to the spectrum for $t \gtrsim 1$ out to well beyond $t_{\max}$ (≈ 9 for $R \gtrsim 500$).

In table 7 we give some values of the least-squares fit of $n(t)$ and $\beta(t)$ for $6 < t < 10$ for the runs at $R = 1600$ and $R = 3000$. These fits are obtained using data from both $13 < k < 83$ and $10 < k < 80$ with $k_{\max} = 84$. In figure 9 we plot $n(t)$ *vs.* t for $R = 1600$ and $R = 3000$. It is apparent that, near $t = 8$, $n(t)$ drops quickly from a value of the order of 3 to a value close to 2. Similar behaviour of $n(t)$ occurs for the run with $R = 1600$. Evidently as t increases toward $t_{\max}$ there is a qualitative change in the character of the high-k spectrum, not inconsistent with the approach to high-k isotropy at these times (cf. figure 8). Also, it can be seen that $n(t)$ has a minimum value close to the Kolmogorov value 1.67 which occurs near $t_{\max}$ when the dissipation rate is maximum.

In figure 10 we give plots of the (least-square) fitted energy spectra for $R = 1600$ and 3000 at $t = 5$ and $t = 8.8$ ($\approx t_{\max}$), both in linear–log and log–log coordinates. We note that $\beta(t_{\max}) = 0.02 \pm 0.01$ for $R = 3000$, while $\beta(t_{\max}) = 0.04 \pm 0.01$ for $R = 1600$; if Kolmogorov-like scaling is present then $\beta = \beta_0(\nu^3/\epsilon)^{\frac{1}{4}}$ gives $\beta_0 \approx 4$.

The least-square fits described above give $A(t_{\max})/\epsilon^{\frac{3}{4}} \approx 4$, which is significantly larger than most experimental measurements of the 'Kolmogorov constant', which give $A/\epsilon^{\frac{3}{4}} \simeq 1.5$. This serious discrepancy can be due to a variety of factors including: (i) the moderate Reynolds numbers of our runs (even at $R = 3000$ the Taylor microscale Reynolds number R_λ at the time of maximum dissipation is only about 110); (ii)

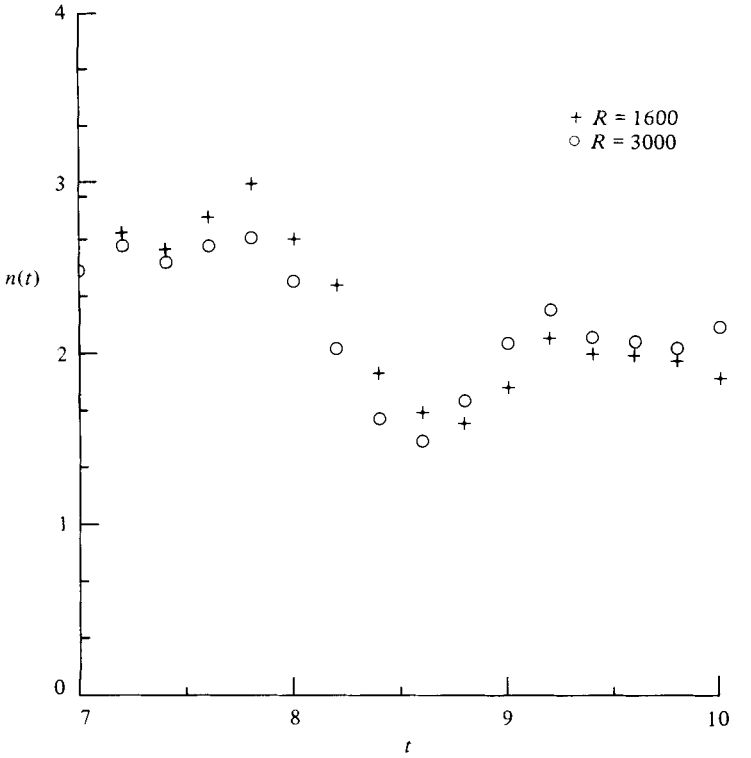

FIGURE 9. Exponent $n(t)$ of the algebraic factor *vs.* t in the spectral fit (5.3). The plus signs are for $R = 1600$; the circles are for $R = 3000$. The least-square fits are done over the wavenumber interval $13 < k < 83$.

the special symmetries of the TG vortex flow; (iii) the high value of $A/\epsilon^{\frac{2}{3}}$ is correlated with a similarly low value of $\epsilon(t_{\max})$. Indeed, $\epsilon(t_{\max}) \approx 10^{-2}$ while the r.m.s. velocity $v_{\rm rms} \approx 0.25$ and the longitudinal integral scale $L_{\rm p} \approx 1.3$ (cf. Orszag 1977) so the fractional energy dissipation per large-eddy turnover time

$$\frac{\epsilon L_{\rm p}}{v_{\rm rms}^3} \approx 0.7, \tag{5.4}$$

which is about a factor 2 smaller than observed in moderate-R_λ wind-tunnel experiments. The relatively weak energy dissipation of the TG vortex may be an indication that only roughly half the volume of the periodicity cube is actively involved in the small-scale turbulence when $t_{\max} \approx 9$ (since ϵ reflects small-scale activity but $L_{\rm p}$ and $v_{\rm rms}$ do not). We return to this point later in this section and in §6 (cf. figure 14). Finally, (iv) our computed high value for the Kolmogorov constant $A/\epsilon^{\frac{2}{3}}$ may simply reflect the effects of intermittency on this constant and its consequent non-universality.

From the spectral analysis just given, we conclude that the TG flow for $t \approx t_{\max}$ when $R > 1000$ does exhibit, at least crudely, inertial-range behaviour with a power-law exponent $n = 1.9 \pm 0.3$, which is weakly dependent on the Reynolds number, and a dissipative wavenumber cutoff that is strongly dependent on R.

Additional analysis of the flow has been done in terms of longitudinal skewness and flatness factors

$$S_n(r) = (-1)^n \frac{\langle [v_x(x+r,y,z) - v_x(x,y,z)]^n \rangle}{\langle [v_x(x+r,y,z) - v_x(x,y,z)]^2 \rangle^{\frac{1}{2}n}}, \tag{5.5}$$

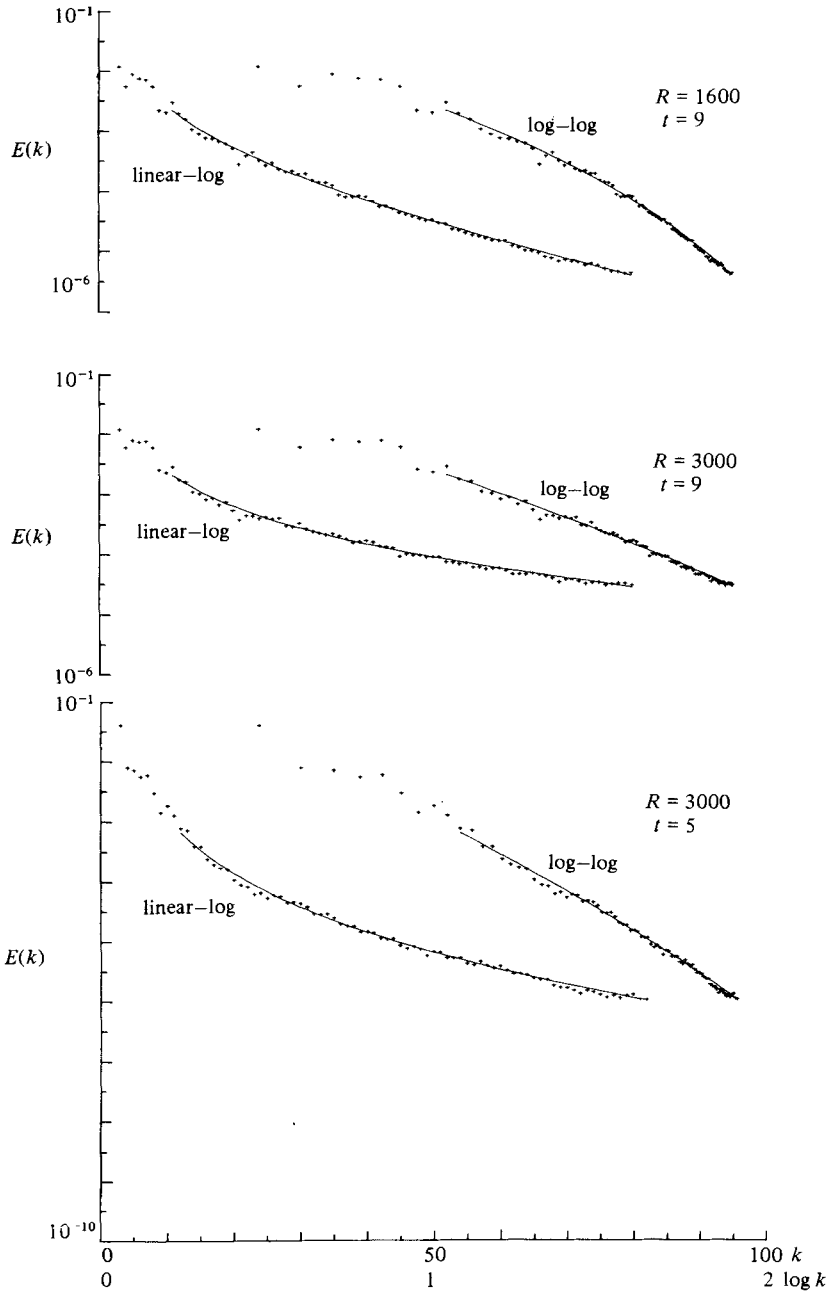

FIGURE 10. Plots of energy spectra $E(k)$ *vs.* k on linear–log and log–log scales: (*a*) $t = 5$, $R = 3000$; (*b*) $t = t_{\max} \approx 9$, $R = 3000$; (*c*) $t = t_{\max} \approx 9$, $R = 1600$. The solid lines are the least-square fits using the assumed form (5.3) over interval $13 < k < 83$.

where $\langle\ \rangle$ now indicates an average over (x, y, z) throughout the spatial periodicity cube. In figure 11, we plot $S_n(r)/S_n(0)$ for $3 \leqslant n \leqslant 6$ for the run with $R = 1600$; we also plot the similarly normalized derivative-flatness factors $\bar{S}_4(r)/\bar{S}_4(0)$ and $\bar{S}_6(r)/\bar{S}_6(0)$ constructed from $\partial v_x/\partial x$ instead of v_x in (5.5). From figure 11, we observe that the higher-order skewness and flatness factors are significantly localized near $r = 0$.

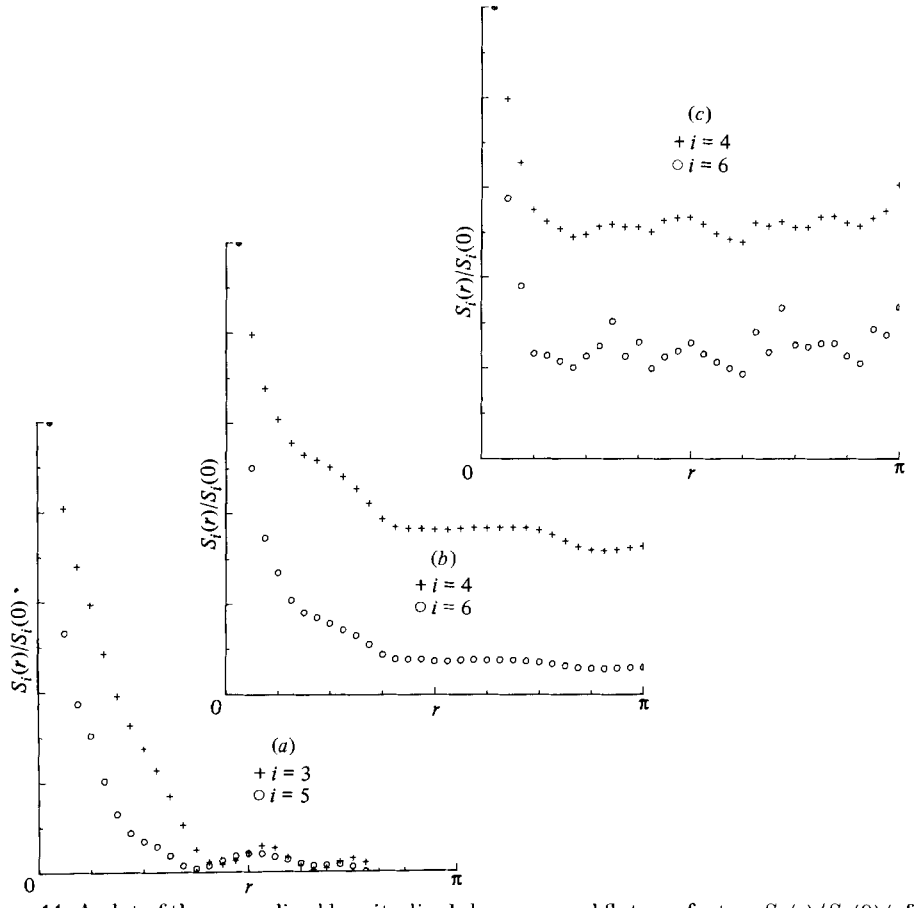

FIGURE 11. A plot of the normalized longitudinal skewness and flatness factors $S_n(r)/S_n(0)$ (cf. (5.5)) *vs.* r for $R = 1600$ at $t = t_{\max} \approx 9$. (*a*) +, S_3; ○, S_5. (*b*) +, S_4; ○, S_6. (*c*) +, $\bar{S}_4$; ○, $\bar{S}_6$.

	R			
	200 ($t = 7$)	400 ($t = 7$)	800 ($t = 7$)	1600 ($t = 9$)
$S_3(0)$	0.45	0.61	0.47	0.65
$S_4(0)$	6.8	6.7	8.8	10.0
$S_5(0)$	9.9	13.9	17.6	23.1
$S_6(0)$	86	99	250	273
$S_8(0)$	1.4×10^3	2.4×10^3	1.4×10^4	1.9×10^4
$\bar{S}_4(0)$	18	17.26	—	15.6
$\bar{S}_6(0)$	773	823	—	660

TABLE 8. Skewness factors (5.6–7)

The values of $S_n(0)$ and $\bar{S}_n(0)$ are given in table 8:

$$S_n(0) = (-1)^n \frac{\langle (\partial v_x/\partial x)^n \rangle}{\langle (\partial v_x/\partial x)^2 \rangle^{\frac{1}{2}n}}, \tag{5.6}$$

$$\bar{S}_n(0) = (-1)^n \frac{\langle (\partial^2 v_x/\partial x^2)^n \rangle}{\langle (\partial^2 v_x/\partial x^2)^2 \rangle^{\frac{1}{2}n}}. \tag{5.7}$$

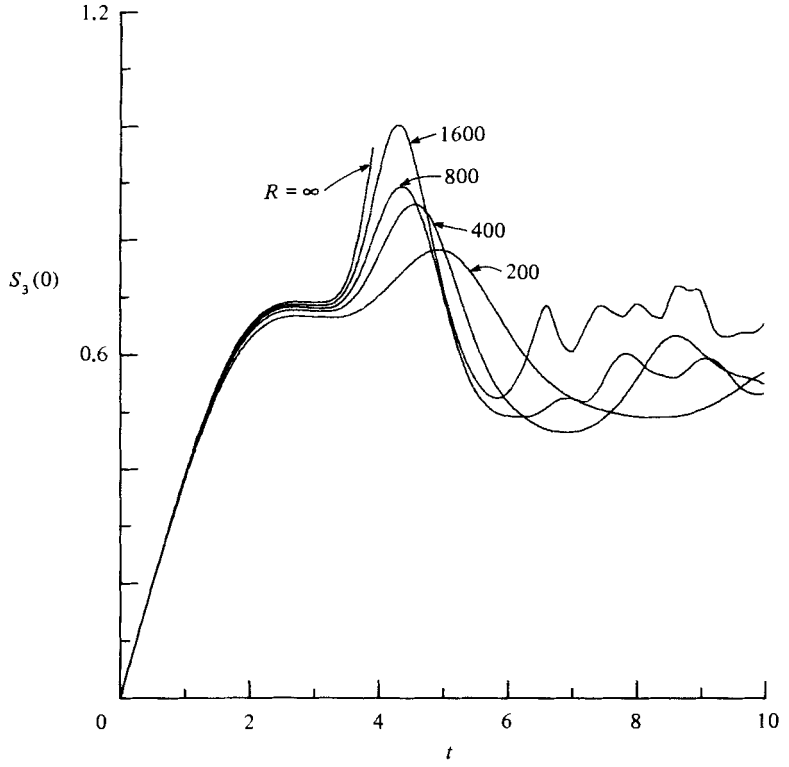

FIGURE 12. A plot of $S_3(0)$ given by (5.6) *vs.* t for $200 \leqslant R \leqslant 1600$. Also plotted is $S_3(0)$ for the inviscid $(256)^3$ run, $R = \infty$ (see §3).

In figure 12, we plot the skewness $S_3(0)$ *vs.* t for various R in the range $200 \leqslant R \leqslant 1600$ as well as $R = \infty$. In this last plot $S_3(0)$ is evaluated by the isotropic relation (cf. Orszag 1977)

$$S_3(0) \doteq \left(\frac{135}{98}\right)^{\frac{1}{2}} \frac{\int_0^\infty k^2 \left.\frac{\partial E}{\partial t}\right|_{\mathrm{NL}} \mathrm{d}k}{\left[\int_0^\infty k^2 E(k)\,\mathrm{d}k\right]^{\frac{3}{2}}}, \tag{5.8}$$

where $\partial E(k)/\partial t|_{\mathrm{NL}}$ is the contribution to $\partial E(k)/\partial t$ due to nonlinear interaction alone (i.e. $\partial E/\partial t|_{\mathrm{NL}} = \partial E/\partial t + 2\nu k^2 E$).

Some comments are in order. First, from figure 12, we conclude that $S_3(0)$ is nearly independent of R for $t \lesssim 3$. Secondly, there is an important qualitative change in the behaviour of $S_3(0)$ near $t = 3$ at large R. In the inviscid flow it follows from (5.8) that

$$S_3(0) = 2\left(\frac{135}{98}\right)^{\frac{1}{2}} \left(-\frac{\mathrm{d}}{\mathrm{d}t}\right) \Omega_1^{-\frac{1}{2}},$$

so that if $S_3(0)$ is positive and does not approach zero rapidly for $t \approx 4$ then Ω_1 would be singular at a finite time. Thus regularity of the Euler flow for all t would require a significant qualitative change in the behaviour of $S_3(0)$ shortly beyond the end of the inviscid curve in figure 12. Thirdly, for $R = 1600$ at $t_{\max}$ the value of $S_3(0)$ calculated by (5.6) is about 0.65, while it is about 0.71 as calculated by (5.8), again signifying the near-isotropy of small scales in this flow. The relatively high value $S_3(0) \approx 0.7$ at $R = 1600$ (compared with experimentally measured values $S_3 \approx 0.4$ at comparable values of R) may also be due to the lack of significant turbulent activity in much of the

periodicity cube. Fourthly, the results given in table 8 show the rapid increase of $\bar{S}_n(0)$ and $\bar{S}_n(0)$ with n, consistent with the strong intermittency of the flow. For example, the values $S_3 \approx 0.7$, $S_4 \approx 10$ at $R = 1600$ are similar to the measurements of Kuo & Corrsin (1971) at $R_\lambda \approx 1000$.

We conclude that there are significant features of the TG flow that mimic laboratory and geophysical flows at much larger Reynolds numbers. If this property persists to higher resolutions and Reynolds numbers, it may be possible to infer the Reynolds-number dependence of skewness and flatness factors using $512 \times 512 \times 512$ or $1024 \times 1024 \times 1024$ calculations of the TG flow, which should be accessible to the next generation of computers.

6. Intermittency and dissipative structure

Intermittency of the small scales of fully developed turbulence may cause deviations from Kolomogorov's original (1941) predictions for pure inertial-range quantities such as the energy-spectrum or velocity-structure functions. However, for such quantities we believe that any deviations that we may observe in our calculations are due much more to insufficiently high Reynolds numbers and/or lack of statistical averaging than to intermittency effects.

Direct access to intermittency is provided by analysing the fluctuations of the local dissipation. The local dissipation is defined as

$$\epsilon(\boldsymbol{r}) = \nu \sum_{i,j} e_{ij}\, e_{ij}, \tag{6.1}$$

where

$$e_{ij} = \frac{1}{2}\left(\frac{\partial}{\partial r_i} v_j(\boldsymbol{r}) + \frac{\partial}{\partial r_j} v_i(\boldsymbol{r})\right). \tag{6.2}$$

Consider the fluctuations in the local dissipation

$$\tilde{\epsilon}(\boldsymbol{r}) = \epsilon(\boldsymbol{r}) - \bar{\epsilon}.$$

According to the original Kolmogorov theory, at inertial-range scales such fluctuations are expressible in terms of velocity fluctuations. These contribute a self-similar process of exponent $\frac{1}{3}$ (Frisch, 1983). Hence the spectrum of dissipation fluctuations $E_\epsilon(k)$ is given, at inertial-range wavenumbers, by

$$E_\epsilon(k) \sim \nu^2\, \bar{\epsilon}^{\frac{4}{3}}\, k^{\frac{5}{3}}. \tag{6.3}$$

In contrast, according to the modified Kolmogorov (1962) theory, dissipation fluctuations may have long-range order, not related to velocity correlations, over distances much larger than the viscous cutoff scale l_{D}. The modified Kolmogorov assumption leads to scaling for the dissipation–fluctuation spectrum:

$$E_\epsilon(k) \sim \bar{\epsilon}^2 (k L_{\mathrm{p}})^{-1+\mu}. \tag{6.4}$$

Here L_{p} is an integral scale and μ is an exponent which in some models has a geometric interpretation as the codimension of a fractal (Mandelbrot 1976; Frisch, Sulem & Nelkin 1978; see also below). The codimension is the dimension of space (three) minus the dimension of the fractal.

Note that the modified Kolmogorov expression (6.4) is by no means a 'deviation' from the original Kolmogorov expression (6.3). Indeed, the former goes to zero with viscosity and not the latter.

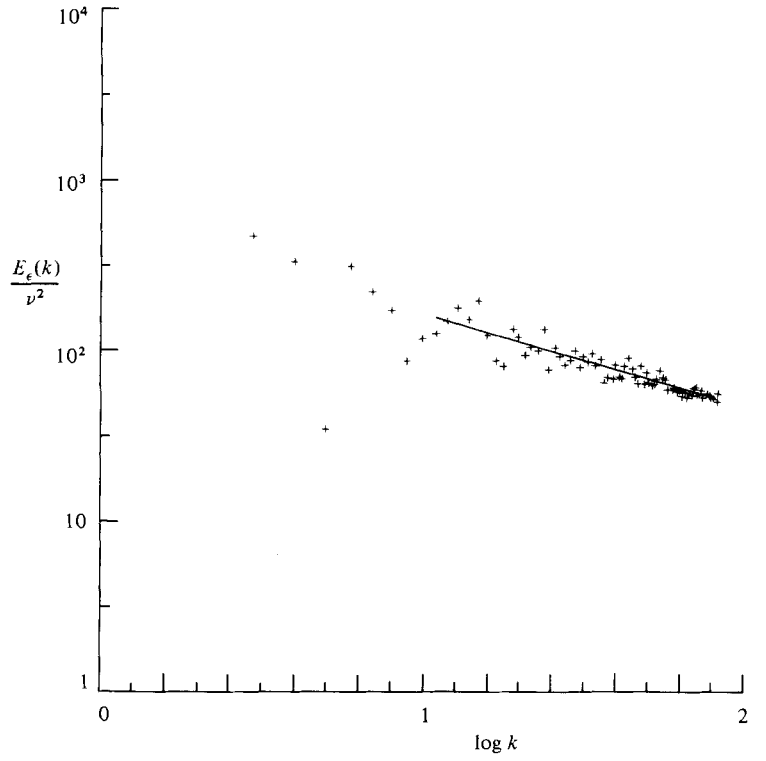

FIGURE 13. A plot of the spectrum of dissipation fluctuations $\epsilon'(\boldsymbol{r})$ given by (6.5) for $R = 3000$ at $t = 9$. The solid line is a least-squares fit to the assumed form (6.4) over the wavenumber interval $11 < k < 83$. The least-square result is $\mu = 0.46$ in (6.4).

We have measured the spectrum of dissipation–fluctuations for the TG vortex. Since the rate-of-strain tensor e_{ij} is not readily accessible in the computer results, we used

$$\epsilon'(\boldsymbol{r}) = \nu\omega^2(\boldsymbol{r}) \tag{6.5}$$

where $\boldsymbol{\omega}(\boldsymbol{r})$ is the vorticity. We note that $\epsilon'(\boldsymbol{r})$ and $\epsilon(\boldsymbol{r})$ have the same integral over space. What is used in experimental studies is neither ϵ nor ϵ' but rather $\epsilon''(\boldsymbol{r}) = \nu(\partial v_x/\partial x)^2$.

In figure 13 we plot in log–log coordinates the spectrum $E_\epsilon(k)$ for $R = 3000$ at $t = 9$; that is, near the time of maximum dissipation. At $R = 3000$ the high-wavenumber tail is essentially a power law. A least-square fit of the kind described in §§3, 5, for $13 < k < 83$, gives

$$\mu = 0.5 \pm 0.2.$$

This result is consistent with experimental data, which are reviewed by Monin & Yaglom (1975). In contrast, a similar plot at $R = 1600$ (not shown) has a very conspicuous dissipation-range exponential tail.

A major advantage of numerical studies of intermittency is that we have access to the full spatial structure of the local dissipation $\nu\omega^2(\boldsymbol{r})$, whereas experimental measurements have had so far access only to the temporal structure (or, at best, to the one-dimensional spatial structure parallel to the mean flow). Contours of $\epsilon'(\boldsymbol{r})$ in various planes of section at $t = 9$ for $R = 3000$ are shown in figure 14. It is apparent that there is significant turbulent excitation over only about half of the impermeable cube, consistent with the result (5.4) for the dimensionless dissipation rate.

In figure 15 we give three-dimensional perspective plots of surfaces inside of which

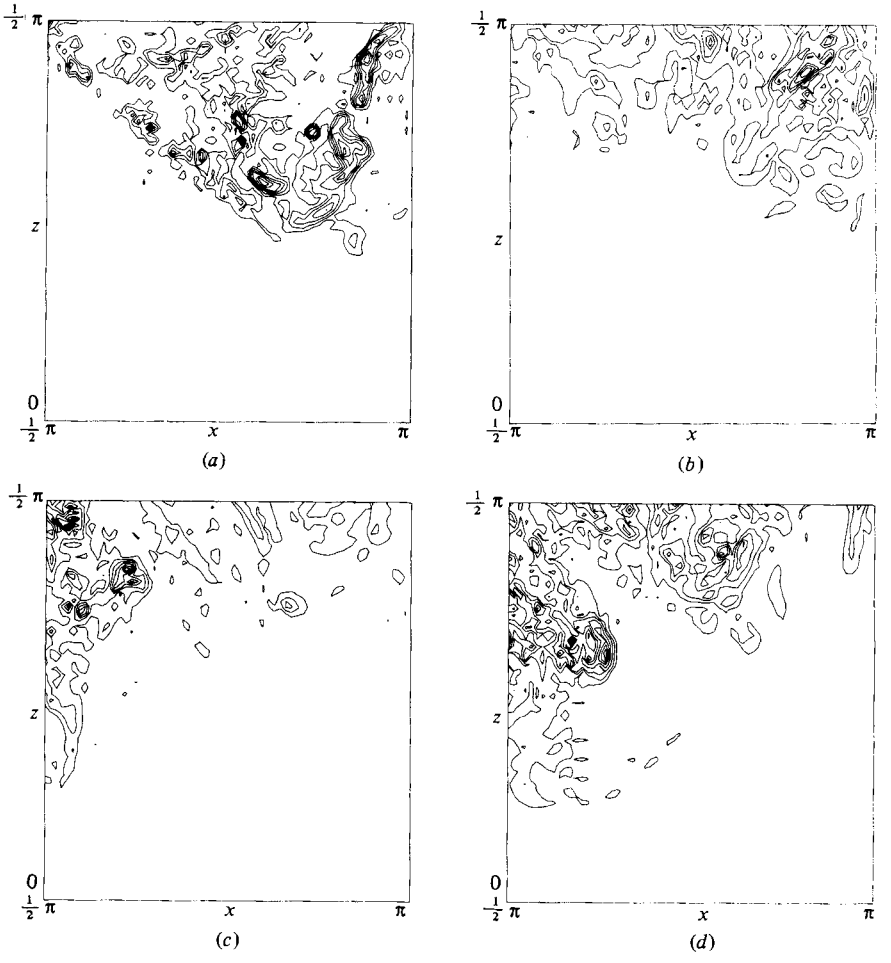

FIGURE 14. Contour plots of local dissipation $\epsilon' = \nu\omega^2(\boldsymbol{r})$ for $R = 3000$ at $t = 9$ in planes $y = y_0$. (*a*) $y_0 = 0$; (*b*) $\frac{20}{128}\pi$; (*c*) $\frac{45}{128}\pi$; (*d*) $\frac{59}{128}\pi$.

the vorticity is larger than some multiple $\gamma\omega_{\max}$ $(0 < \gamma < 1)$ of its maximum $\omega_{\max}$ over the cube. The results for the inviscid run at $t = 4.1$ with $\gamma = \frac{1}{2}$ (figure 15*a*) show the relatively simple topological structure of high-vorticity regions in the inviscid flow at this moderate time. The results for $R = 3000$ at $t = 7$ with $\gamma = \frac{1}{2}$ (figure 15*b*) are somewhat more complicated topologically, while those for $R = 3000$ at $t = 9.5$ ($\gamma = \frac{1}{2}$ in figure 15*c*, $\gamma = 0.7$ in figure 15*d*) are exceedingly complicated. Comparison of figure 15(*c*) with figure 15(*a*, *b*) shows that for the same γ (here $\frac{1}{2}$) the volume enclosed is much larger and dispersed at $t = 9.5$ than at the earlier times. Comparison of figure 15(*d*) with figure 15(*b*) shows that for fixed amplitude $\gamma\omega_{\max}$ the enclosed volume is only slightly smaller at $t = 7$ than at $t = 9.5$ (as also follows from the similarity of Ω_1 at these two times), but the regions of high $|\omega|$ are considerably more intermittent at $t = 9.5$. We mention that, while Ω_1 only achieves its maximum at $t \approx 9$, $\omega_{\max}$ reaches its maximum at the earlier time $t \approx 7$ for $R = 3000$. This may reflect the initial dominance of vortex stretching and enhancement before equilibrium turbulent structures evolve, and then the effect of finite Reynolds number in the generation of spatial intermittency.

Visualizing small-scale activity by the strength of vorticity can have shortcomings. Indeed a large but nearly uniform vorticity may be solid-body rotation, which has

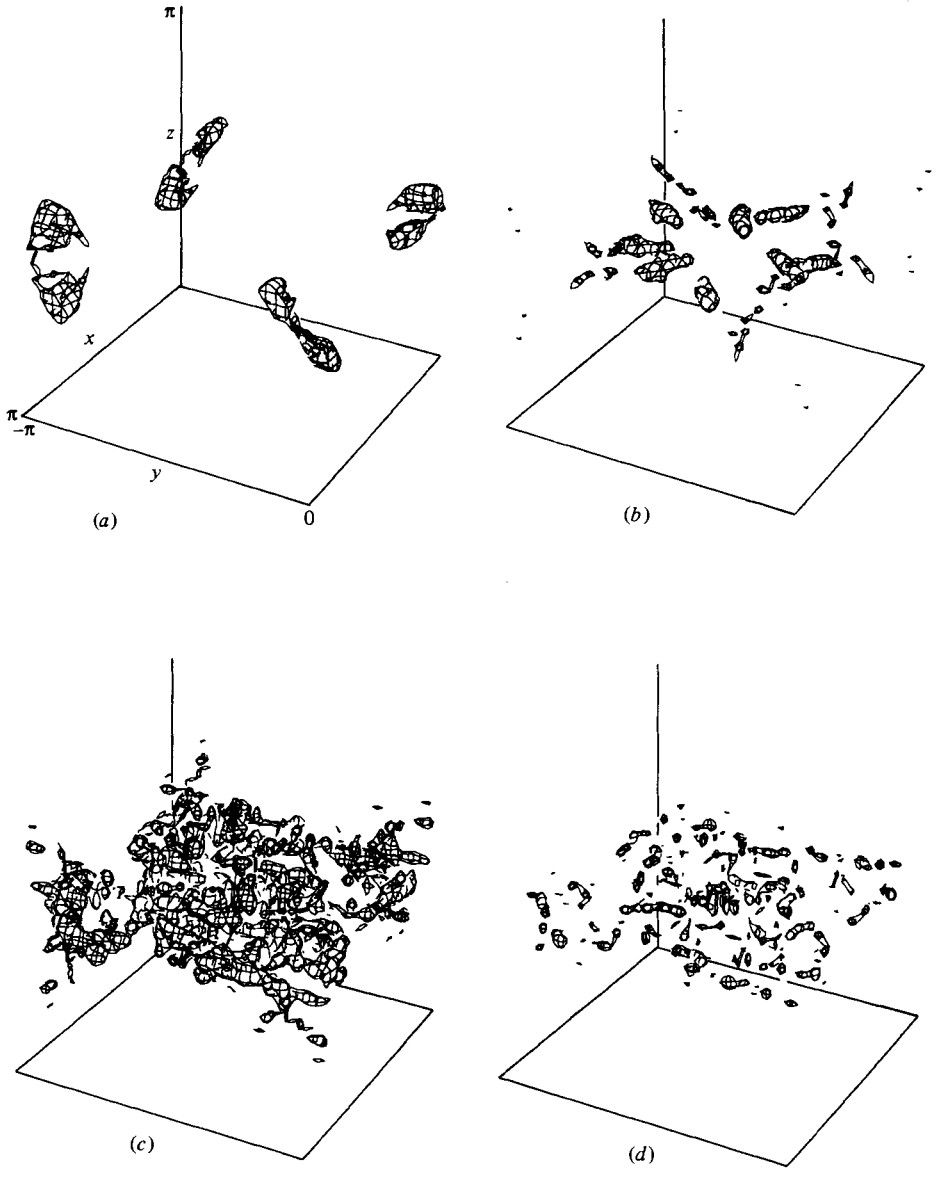

FIGURE 15. Three-dimensional perspective plots of surfaces in which $|\omega(\boldsymbol{r})| > \gamma\omega_{\max}$, where $\omega_{\max} = \max_{\boldsymbol{r}}|\omega(\boldsymbol{r})|$. (*a*) Inviscid run at $t = 4.1$, $\omega_{\max} = 18.3$, $\gamma\omega_{\max} = 9.2$. (*b*) $R = 3000$, $t = 7$, $\omega_{\max} = 33.7$, $\gamma\omega_{\max} = 16.8$. (*c*) $R = 3000$, $t = 9.5$, $\omega_{\max} = 24.2$, $\gamma\omega_{\max} = 12.1$. (*d*) $R = 3000$, $t = 9.5$, $\omega_{\max} = 24.2$, $\gamma\omega_{\max} = 16.9$.

a very strongly dispersive action and thereby inhibits the formation of small-scale structures. We remark also that, in numerical simulations of small-scale turbulence, Siggia (1981) found that the regions of high vorticity and of high rate of strain are not quite the same.

It has been conjectured that in the limit $\nu \downarrow 0$ all the dissipation concentrates in a fractal (Mandelbrot 1976). It then follows that $E_\epsilon(k)$ follows a power law of the form (6.4), where μ is the Fourier codimension (Kahane 1976). In our calculation at $R = 3000$, power-law behaviour is obtained in the highest wavenumber octave. This

corresponds to roughly one mesh in physical space, so that we cannot expect to see any fractal-like structures. Furthermore, scaling for $\nu \downarrow 0$ in Fourier space does not necessarily imply the existence of a limit (however weak) in physical space for unaveraged quantities, so generalizations of the fractal concepts may be required. Actually the only proven mathematical result relating fractals and high-Reynolds-number flow is the obtained theorem of Cafarelli, Kohn & Nirenberg (1981), which improves previous results by Scheffer (1975): in four-dimensional space–time, the set of points where viscous flow is singular (with unbounded velocity) has Hausdorff dimension not greater than one.

For the TG vortex with $R < 1000$, analyticity in the space variables, as evidenced by an exponential tail in the energy spectrum, is likely to hold for all times; thus the singular set may be empty.

7. Time evolution of the viscous TG flow: the transition to turbulence

In §§5 and 6 we have concentrated on studying the flow near the time $t_{\max}$ of maximum dissipation when it is most likely to display features of fully developed turbulence.

At the highest Reynolds numbers used ($R = 1600$ and 3000), the flow remains essentially inviscid up to about $t = 3.5$. At such early times the energy spectrum has, over a substantial fraction of the wavenumber range, a power-law behaviour (see §3). The spectral exponent n is of the order of 4, much larger than the Kolmogorov $\frac{5}{3}$ value. At subsequent times the spectrum is somewhat shallower. The spectral exponent n, determined by least-square fit of the log of the energy spectrum, fluctuates around 3 until about $t = 8$, when it quite suddenly drops to values not inconsistent with the Kolmogorov spectrum (see figure 9).

To understand what is happening we have made extensive flow visualizations using two-dimensional sections and three-dimensional perspective plots. The run at $R = 1600$ was used in order to get sufficiently smooth features of small-scale vorticity. The results are shown in figures 16–19. The following sequence of events is observed. The initial quasi-inviscid evolution leads to the formation around $t = 4$ of vortex sheets and daughter vortices as discussed in §2. Substantial roll-up of the vortex sheets has occurred by $t = 5$; this flow pattern remains qualitatively unchanged through $t = 6$ (figure 16). Then, by $t = 7$, the rolled-up sheets undergo violent topological changes (probably involving viscous rearrangement of vortex lines). As a consequence very disordered high-vorticity patches appear in a substantial fraction of the impermeable cube. We then have a flow in which coherent vortex structures located near the walls of the impermeable cube coexist with very disordered high-vorticity patches away from the walls. The coherent structure itself finally breaks down around $t = 8$. The sudden change around $t = 7$ is also manifest in figure 20, in which we plot, for various times, the maximum of the vorticity as a function of the distance to the walls.

We observe that eventually the viscous TG flow will decay to zero at all Reynolds numbers because it is not subject to any forcing. Hence there cannot be any *temporal* chaos because this would require a non-trivial attractor as $t \to \infty$. Nevertheless, a kind of transition to spatial chaos, controlled by the time parameter, seems to manifest itself in the high-Reynolds-number TG flow. At early times the flow is highly organized, i.e. 'laminar'; around $t = 7$ it becomes 'turbulent', displaying a mixture of order and chaos! Note that we are here using 'laminar' and 'turbulent' as commonsense notions, postponing a more precise definition.

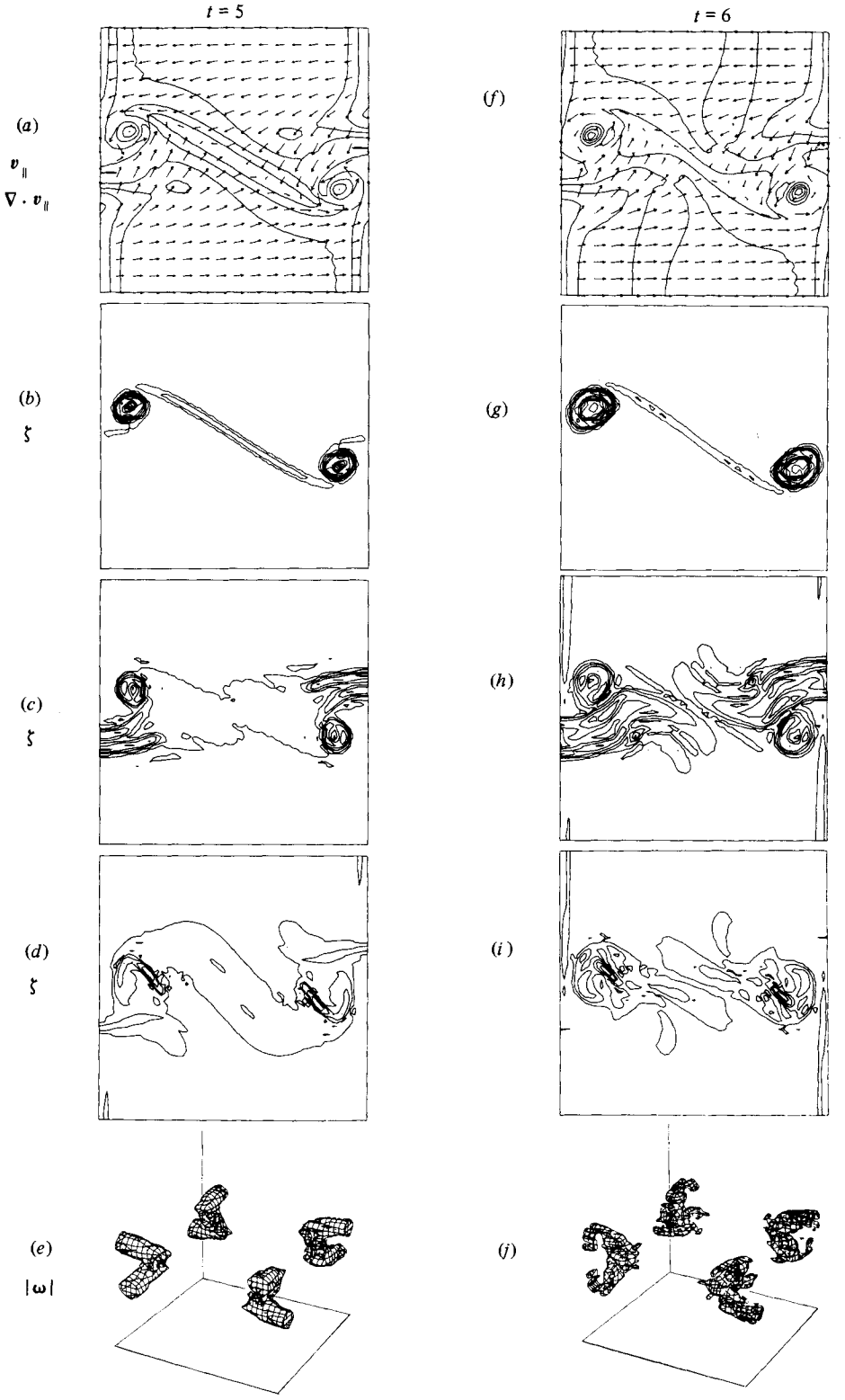

FIGURE 16. For caption see facing page.

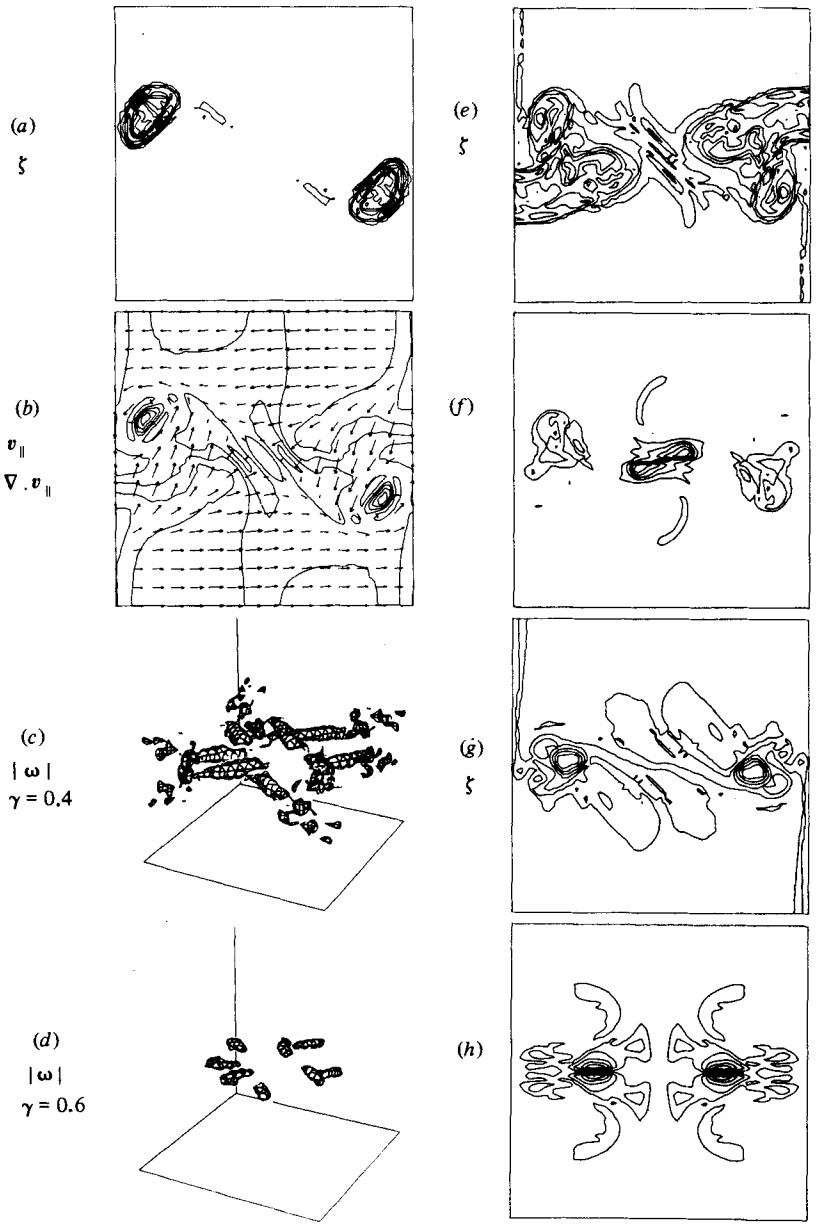

FIGURE 17. Flow visualizations at $t = 7$. (*a*), (*e*)–(*h*) show vorticity contours in the planes $y = 0$, $\frac{1}{8}\pi$, $\frac{1}{4}\pi$, $\frac{3}{8}\pi$, $\frac{1}{2}\pi$ respectively. (*b*) shows velocity vectors and strain-rate contours in the plane $y = 0$. (*c*), (*d*) are three-dimensional perspective plots as in figure 15 with $\gamma = 0.4$, 0.6 respectively. Here $R = 1600$.

Some tentative scenarios for this transition to turbulence are now given. The high-Reynolds-number and short-time behaviour is essentially inviscid. Up to about $t = 2.5$ the inviscid dynamics produce well-organized small-scale structures near the impermeable walls. Their characteristic scale δ decreases exponentially, at least up

FIGURE 16. Flow visualizations at $t = 5$ and $t = 6$. (*a*) and (*f*) (as in figure 1) give velocity vectors and strain-rate contours in the plane $y = 0$ at $t = 5$, 6 respectively. (*b*)–(*d*) and (*g*)–(*i*) give contours of vorticity in the planes $y = 0, \frac{1}{8}\pi, \frac{1}{4}\pi$ respectively at $t = 5$ and $t = 6$. (*e*) and (*j*) are three-dimensional perspective plots of surfaces in which $|\omega(r)| > 0.4\omega_{\max}$ at $t = 5$, 6. Here $R = 1600$.

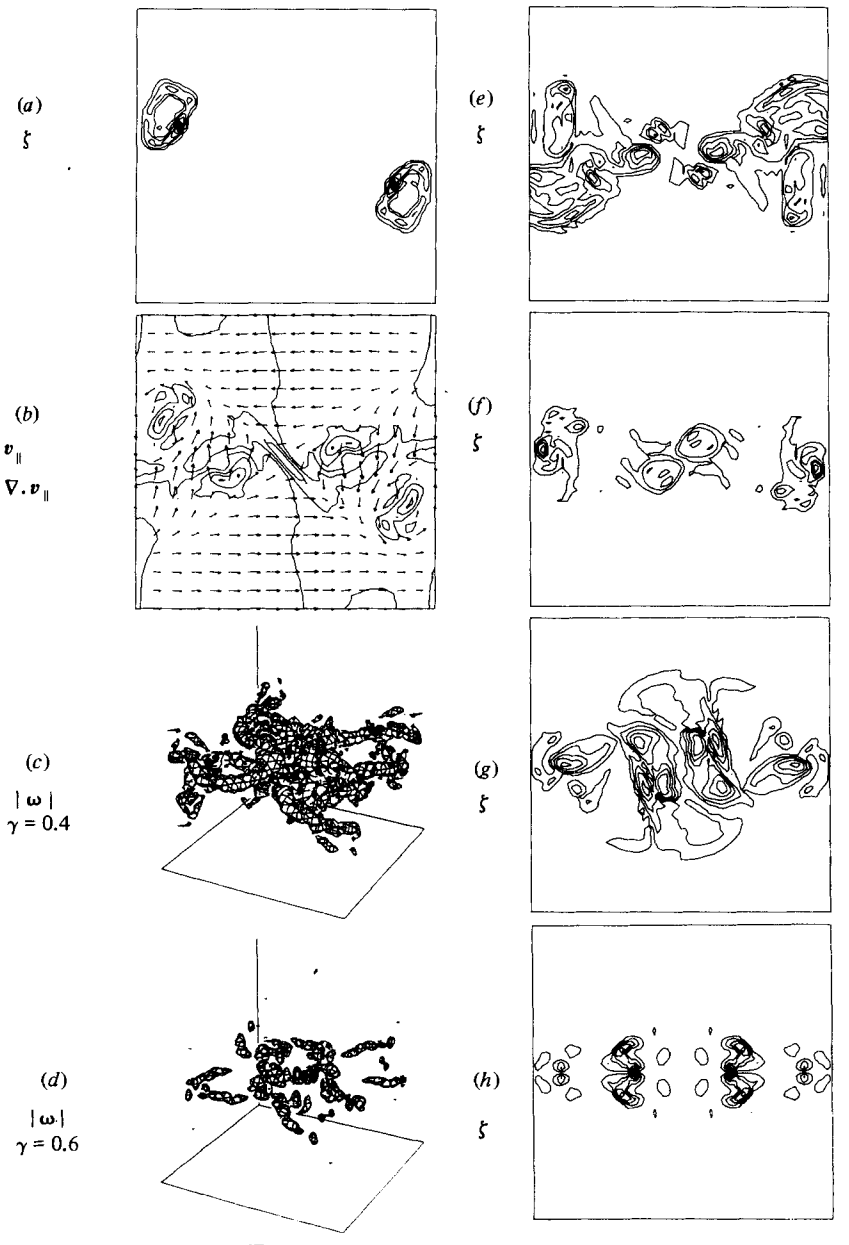

FIGURE 18. Same as figure 17 except $t = 8$.

to the time where it becomes comparable to the mesh of our simulation (figure 5). After that we are faced with two possibilities.

(a) *Laminar inviscid flow – viscosity-induced instabilities*

In the inviscid flow, the exponential flattening may go on forever. In the viscous case, the flattening will then proceed until stopped by viscous diffusion or by some instability. If viscous diffusion persists, the smallest attained scale l may be estimated by equating the e-folding time $T \approx 0.57$ (from (3.6)) and the viscous decay time

$$t_{\text{visc}} \sim (\nu k^2)^{-1}, \quad k = \frac{2\pi}{l}. \tag{7.1}$$

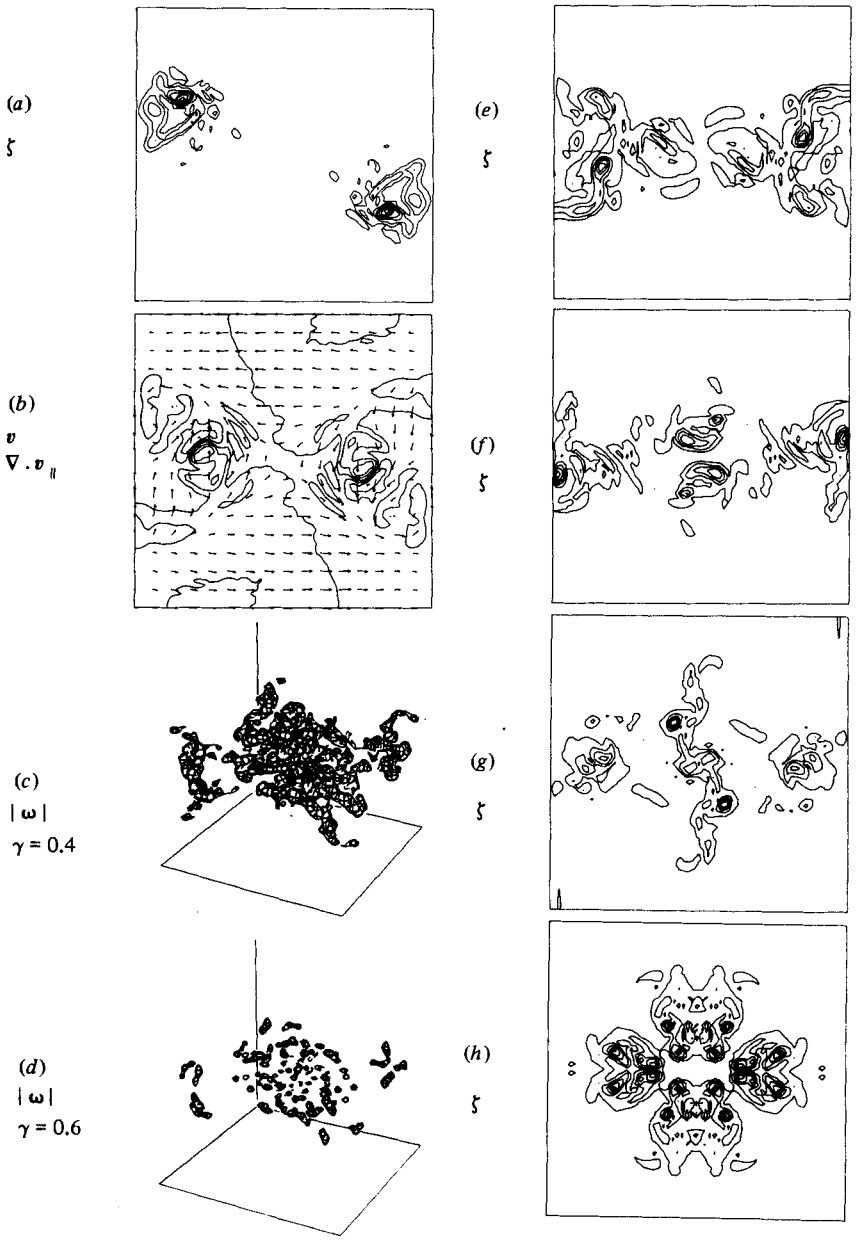

FIGURE 19. Same as figure 17 except $t = 9$.

Thus, for $\nu = (3000)^{-1}$, flattening stops at a scale of a few meshes. On the other hand, at $t = 9$, we observe convoluted high-vorticity patches extending over much more than a few meshes (figure 14). We conclude that there may be viscosity-induced instabilities. The latter may then trigger inviscid instabilities leading by a sort of inverse cascade process to the observed inertial-range scales.

(*b*) *Turbulent inviscid flow*

In the inviscid flow there may be a genuine crossover to more violent behaviour involving Kelvin–Helmholtz or other inviscid instabilities, as discussed at the end

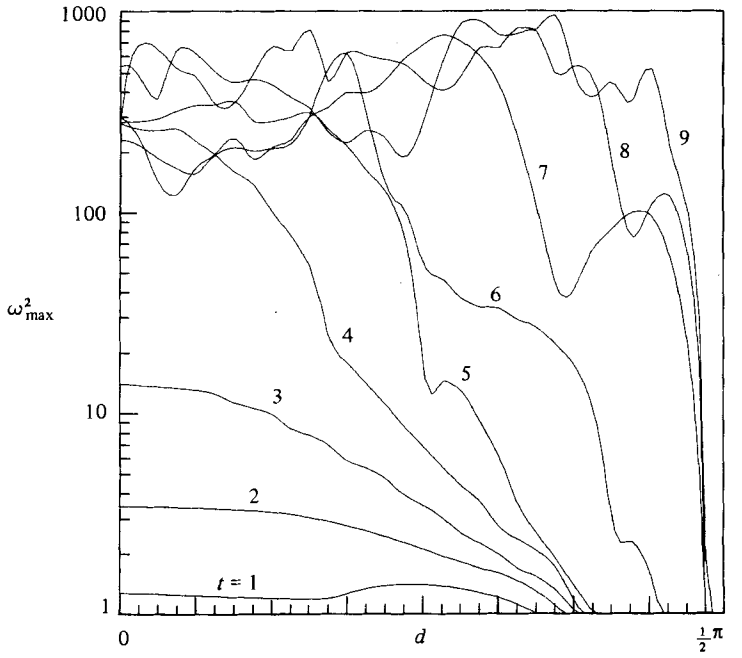

FIGURE 20. A plot of the maximum vorticity ω^2_{max} as a function of the distance from the walls of the impermeable cube for $t = 1$–9 (1). Here we compute ω^2_{max} over the faces of subcubes nested in such a way that the distance from the nearest wall of the impermeable cube is d. Thus $d = 0$ corresponds to the maximum vorticity on the faces of the impermeable cube while $d = \frac{1}{2}\pi$ corresponds to the vorticity at the centre of this cube. Observe that for early times the vorticity is concentrated near the walls of the impermeable cube. As t increases beyond 6, there is significant vorticity generation in the main body of the cube.

of §2. Viscosity, as it comes into play, will prevent any singularities that might otherwise have formed; viscosity may allow inviscidly formed structures to coalesce into larger ones; and may also induce new instabilities.

Neither of the above scenarios agrees with the one immortalized in Richardson's version of Swift's poem, because the latter has inertial-range structures being formed by a cascade from larger to smaller scales. This may not matter, for Richardson did not mean to describe transient stages of decaying turbulence.

It is of considerable interest to point out that scenario (*a*) is actually taking place in high-Reynolds-number two-dimensional magnetohydrodynamic (2-D MHD) turbulence. In 2-D MHD flow, the exponential flattening process, near neutral magnetic-X points, is probably going on forever in the inviscid case, as evidenced by numerical simulations (at resolutions up to 512^2) and by asymptotic expansions (Frisch *et al.* 1983). The resulting sheet-like structures are then subject to resistive tearing-mode instabilities leading to the formation of magnetic islands (Furth, Killen & Rosenbluth 1963). At high R the resulting unstable flow is quite complicated, intermittent and turbulent.

In the context of MHD, but in three dimensions, a definition of 'turbulence' is often used that involves only the instantaneous topology of magnetic-field lines without any reference to the time variable. The topology is said to be chaotic or turbulent if the Poincaré map (successive intersections of field lines with a transverse surface) is non-integrable or, equivalently, if field lines emanating from neighbouring points may diverge exponentially (as a function of arclength). A very simple example of topological turbulence is given by Hénon (1966).

Returning to the three-dimensional TG flow, we propose to carry over the above definition of topological turbulence† in terms of the vortex lines. The latter seem preferable to streamlines because the topology of vortex lines can change only by viscous reconnection. The TG flow is initially topologically laminar, because it has closed vortex lines and it remains so under inviscid evolution (as long as the flow is smooth). At early times, before appreciable small-scale structure has been generated, a small amount of viscous diffusion can make the flow topologically turbulent, but only slightly so. At later times violent reconnection may take place, possibly leading to strong topological turbulence. A quantitative measure of the strength can be based on Lyapunov exponents and Kolmogorov entropy (Benettin, Galgani & Strelcyn 1976). In this way, concepts that are generally used in connection with dynamical systems having only a few degrees of freedom may become useful for studying transition to fully developed turbulence, with time playing the role of the bifurcation parameter.

We would like to thank Dr A. T. Patera for assistance with the algorithms and design of the time-dependent spectral code. We would also like to thank Drs R. H. Kraichnan, B. Mandelbrot, W. V. R. Malkus, R. L. McCrory, R. Pellat, P.-L. Sulem and J. Weiss for helpful discussions. Last, but certainly not least, we would like to thank N. T. Jones, Jr for considerable assistance with the graphics; he is also responsible for a striking computer-generated ciné film of the TG vortex. The time-dependent computations were performed on the Cray-1 computer at the National Center for Atmospheric Research, which is sponsored by the National Science Foundation; the series computations were done on the Amdahl V/5 computer at the University of Guelph. This work was supported by the National Science Foundation under Grants ATM-8017284 and DMR-77-10-10120, the Office of Naval Research under Contracts N00014-77-C-0138 and N00014-79-C-0478, the NSERC of Canada, and the A. P. Sloan Foundation. Finally, U.F., B.G.N. and R.H.M. would like to acknowledge the hospitality of the Department of Physics, Harvard University, where much of this work was done.

Appendix A. Symmetries of the TG flow

The planes $x, y, z = n\pi$ are stress-free and mirror-symmetric for all time and any values of θ in the initial conditions (1.1). Given the flow inside the impermeable box at time t, one can determine the flow everywhere in the full periodicity box by reflection about these planes. For example,

$$\left.\begin{aligned} v_x(-x,y,z,t) &= -v_x(x,y,z,t), \\ v_i(-x,y,z,t) &= v_i(x,y,z,t) \quad (i=y,z) \end{aligned}\right\} \tag{A 1}$$

follows directly from the mode decomposition (1.2). In addition, the flow within the impermeable box is invariant under rotations of π about any of the three axes $x = y = \frac{1}{2}\pi$, $x = z = \frac{1}{2}\pi$, or $y = z = \frac{1}{2}\pi$. For example,

$$\left.\begin{aligned} v_x(\pi-x,\pi-y,z,t) &= -v_x(x,y,z,t), \\ v_y(\pi-x,\pi-y,z,t) &= -v_y(x,y,z,t), \\ v_z(\pi-x,\pi-y,z,t) &= v_z(x,y,z,t) \end{aligned}\right\} \tag{A 2}$$

† 'Tohu-Bohu', which describes the early state of the Universe (Genesis 1.2), might be a convenient substitute for 'topological turbulence'.

also follows from the mode decomposition (1.2) when explicit use is made of the restriction that m, n and p in any one mode differ by even integers.

For special values of θ there exist relationships among the expansion coefficients corresponding to additional symmetries within the impermeable box. For $\theta = 0$,

$$\left.\begin{aligned} u_x^{(r)}(m,n,p) &= (-1)^{r+1}\, u_y^{(r)}(n,m,p), \\ u_z^{(r)}(m,n,p) &= (-1)^{r+1}\, u_z^{(r)}(n,m,p), \end{aligned}\right\} \tag{A 3}$$

and the flow for all time is invariant under rotation by $\frac{1}{2}\pi$ about the vertical axis $x = y = \frac{1}{2}\pi$, i.e.

$$\left.\begin{aligned} v_x(y,\pi-x,z,t) &= v_y(x,y,z,t), \\ v_y(y,\pi-x,z,t) &= -v_x(x,y,z,t), \\ v_z(y,\pi-x,z,t) &= v_z(x,y,z,t). \end{aligned}\right\} \tag{A 4}$$

For $\theta = \frac{1}{2}\pi$

$$\left.\begin{aligned} u_x^{(r)}(m,n,p) &= u_y^{(r)}(n,m,p), \\ u_z^{(r)}(m,n,p) &= u_z^{(r)}(n,m,p), \end{aligned}\right\} \tag{A 5}$$

and the flow within the impermeable box is now divided into four isolated volumes separated by mirror planes $x = y$ and $x = \pi - y$. This symmetry in coordinate representation is

$$\left.\begin{aligned} v_x(y,x,z,t) &= v_y(x,y,z,t), \\ v_z(y,x,z,t) &= v_z(x,y,z,t). \end{aligned}\right\} \tag{A 6}$$

Appendix B. Numerical methods and data management

The Navier–Stokes equations

$$\frac{\partial \boldsymbol{v}}{\partial t} = \boldsymbol{v} \times \boldsymbol{\omega} - \nabla(p + \tfrac{1}{2}v^2) + \nu \nabla^2 \boldsymbol{v}, \tag{B 1}$$

$$\nabla \cdot \boldsymbol{v} = 0, \tag{B 2}$$

where $\boldsymbol{\omega} = \nabla \times \boldsymbol{v}$, p is the pressure and ν is the kinematic viscosity, are solved using spectral methods based on the special representation (1.2) truncated to $0 \leqslant m \leqslant M$, $0 \leqslant n \leqslant N$, $0 \leqslant p \leqslant P$. The nonlinear terms are evaluated pseudospectrally taking advantage of all the special symmetries of the TG vortex listed in appendix A. For this purpose, a new odd Fourier transform algorithm was devised (see appendix C). For M, N, P that are powers of 2, the nonlinear terms are evaluated in order $MNP \log_2 MNP$ operations; all the symmetries are utilized so this evaluation proceeds 64 times faster and with 64 times less memory than would be required by a full complex Fourier-series representation of a general asymmetrical, spatially periodic flow. In practice, our TG code runs about half as fast as a general pseudospectral code with $\frac{1}{2}M \times \frac{1}{2}N \times \frac{1}{2}P$ complex Fourier-series resolution, and requires about 50 % more data transfers.

In the text, runs with $M = N = P = 128$ are denoted $(256)^3$ as the equivalent complex Fourier series involves $(256)^3$ terms. While the representation (1.2) is a sparse spectral representation with many complex Fourier modes required to have zero amplitude, the ratio of largest to smallest wavenumber component is 128, the same as for a general $(256)^3$ spectral code. The sparse spectral representation of the TG flow is a cheap and convenient way to get enhanced small-scale resolution; indeed, the TG code with $(256)^3$ resolution is roughly equivalent to a $(64)^3$ general spectral code as far as computational work and storage.

Time-stepping is done by second-order leapfrog differencing for the nonlinear terms and second-order Crank–Nicolson implicit differencing for the viscous terms. The pressure is eliminated by algebraic manipulation of the incompressibility constraint (B 2) in Fourier representation. The aliasing terms that result from the pseudospectral algorithm are removed by spectral truncation (Orszag 1971). With $M = N = P$, aliasing removal gives the largest wavenumber component $k_{\max} \approx \frac{2}{3}M$. With $M = 32$, $k_{\max} = 20$; with $M = 64$, $k_{\max} = 42$; with $M = 128$, $k_{\max} = 84$.

A variety of accuracy checks have been made. At $R = 400$, comparisons of spectra, generalized enstrophies (see (3.1)), and skewnesses (see (5.6)) at $t_{\max}$ indicate that the $(128)^3$ code gives results accurate to better than 1 % for all significant scales, while the $(64)^3$ code has errors of order 5 % and the $(32)^3$ is in error by 20–50 % at small scales. Assuming Kolmogorov scaling (in which the dissipation cutoff wavenumber scales as $R^{\frac{3}{4}}$) holds approximately for $R \gtrsim 400$ (cf. §5), we conclude that the $(256)^3$ code is in error by a few per cent at $R = 1600$ and by order 10 % at $R = 3000$ at $t_{\max}$.

Perhaps the most involved aspect of our code is its data-management scheme. For the $(256)^3$ runs, each velocity component of the TG vortex involves $2^{19} \approx 0.5$ M independent real degrees of freedom. With the available memory of about 0.8 M words on the NCAR Cray-1, it is necessary to use secondary (disc) storage to supplement main memory. As our code uses a relatively novel data-management scheme to achieve both minimal data transfers and maximal data throughput, we outline the scheme briefly here.

Data is segmented (blocked) in terms of the y- and z-coordinates of arrays; individual blocks are always complete in the x-direction. An individual block involves B_y values in the y-direction, and B_z values in the z-direction with the all-odd and the all-even Fourier components (and their contribution to physical space fields) segregated into separate arrays in the same block. Thus there are $(M+2)\,B_y\,B_z$ real values in each data block. With the $(256)^3$ code on the NCAR Cray-1, we choose $B_y = B_z = 17$, so there are four blocks in each of the y- and z-directions.

The code involves two stages.

Stage 1. $[(N+2)/2B_y]$ blocks with fixed z are assembled to form complete (x, y)-arrays. The data inputted to this stage from disc are v_x, v_z and ω_y in the mixed spectral representation in which x and y are in Fourier representation while z is in physical representation. The data output from this stage to disc are $(\boldsymbol{v}\times\boldsymbol{\omega})_x$, $(\boldsymbol{v}\times\boldsymbol{\omega})_z$ and $\boldsymbol{\nabla}_{\mathrm{H}}\cdot(\boldsymbol{v}\times\boldsymbol{\omega})$, where $\boldsymbol{\nabla}_{\mathrm{H}} = (\partial/\partial x, \partial/\partial y, 0)$, in the same mixed representation as on input.

Stage 2. $[(P+2)/2B_z]$ blocks with fixed y are assembled to form complete (x, z)-arrays. Input fields are $(\boldsymbol{v}\times\boldsymbol{\omega})_x$, $(\boldsymbol{v}\times\boldsymbol{\omega})_z$, $\boldsymbol{\nabla}_{\mathrm{H}}\cdot(\boldsymbol{v}\times\boldsymbol{\omega})$ for the current time step, and v_x, v_z from the previous time for leapfrog time differencing; output fields are v_x, v_z and ω_y at the next time level. All data is stored in mixed spectral representation on disc.

Asynchronous data transfer between disc and central memory is done using 4 simultaneous data channels to achieve optimal data-transmission rates. Block (j, k) with $1 \leqslant j \leqslant [(N+2)/2B_y]$, $1 \leqslant k \leqslant [(P+2)/2B_z]$ is stored on a disc attached to channel $j-k \pmod 4 + 1$ for stage 1 input and stage 2 output and $k-j \pmod 4 + 1$ for stage 1 output and stage 2 input. This scheme minimizes repositioning time.

Some characteristics of the codes are given in table 9.

Resolution	Block width B_y	Block width B_z	Central memory (10^6 words)	Block size (10^4 words)	Data transfers per time step (10^6 words)	CPU time/step (s)	I/O wait time/step (s)	Typical time step
256^3	17	17	0.61	3.81	8.5	9.1	5	0.005
†512^3	11	11	1.51	3.15	63.4	84	45	0.002
‡1024^3	26	26	13.9	34.9	488	75	40	0.001

† With this choice of B_y and B_z, the Cray-1 computer must have at least 2×10^6 words of memory.
‡ Estimates for a hypothetical class VII computer (*ca.* 1985) with 16 M+ words of memory, and CPU capability and I/O bandwidth ten times that of the Cray-1 computer.

TABLE 9. Computer storage and timings

Appendix C. Fast transform of odd Fourier series

The pseudospectral method for solution of the TG flow requires the evaluation of the discrete Fourier transforms

$$A_j = \sum_{n=0}^{N} a_n \begin{Bmatrix} 2\cos 2nx_j \\ 2\mathrm{i}\sin 2nx_j \end{Bmatrix} \quad (0 \leqslant j \leqslant N), \tag{C 1}$$

$$A_j = \sum_{n=0}^{N-1} a_n \begin{Bmatrix} 2\cos(2n+1)x_j \\ 2\mathrm{i}\sin(2n+1)x_j \end{Bmatrix} \quad (0 \leqslant j \leqslant N), \qquad \begin{matrix} (\mathrm{C}\ 2a) \\ (\mathrm{C}\ 2b) \end{matrix}$$

where $x_j = \pi j/2N$ $(0 \leqslant j \leqslant N)$, as well as evaluation of their inverse transforms for a_n in terms of A_j. Here N is a power of 2. The transform (C 1) and its inverse is immediately reducible to a standard discrete cosine or sine transform that can be evaluated by a single fast Fourier transform on N points (see appendix II of Orszag 1971). In this appendix, we explain how to reduce the evaluation of (C 2) and its inverse to a single fast Fourier transform on N points (rather than its obvious expression as a $2N$-point transform).

First we remark that $A_N \equiv 0$ with (C 2a) and $A_0 \equiv 0$ with (C 2b), so there are only N independent results among A_j $(0 \leqslant j \leqslant N)$, matching the N independent a_n $(0 \leqslant n < N)$. Next we introduce $\bar{a}_n$ by

$$\bar{a}_n = \begin{Bmatrix} a_n & (0 \leqslant n \leqslant N-1), \\ \delta a_{2N-n-1} & (N \leqslant n \leqslant 2N-1), \end{Bmatrix} \tag{C 3}$$

where $\delta = +1$ for the cosine transform (C 2a), while $\delta = -1$ for the sine transform (C 2b). Then

$$A_j = \sum_{n=0}^{2N-1} \bar{a}_n \mathrm{e}^{\mathrm{i}(2n+1)x_j}. \tag{C 4}$$

Next we set

$$b_n = \bar{a}_{2n} \quad (0 \leqslant n < N), \tag{C 5}$$

with $\bar{a}_{-1} = \bar{a}_{2N-1}$ and

$$B_j = \sum_{n=0}^{N-1} b_n \mathrm{e}^{2\pi\mathrm{i}jn/N} \quad (0 \leqslant j < N). \tag{C 6}$$

Then B_j can be evaluated by a single N-point fast Fourier transform. A little algebra then shows that

$$A_j = \mathrm{e}^{\mathrm{i}x_j} B_j + \delta \mathrm{e}^{-\mathrm{i}x_j} B_{N-j} \quad (0 \leqslant j \leqslant N), \tag{C 7}$$

with $B_N = B_0$. Equation (C 7) is derived noting that $\bar{a}_{2N-n} = \delta \bar{a}_{n-1}$ $(1 \leqslant n \leqslant 2N-1)$.

The inverse transform to (C 2) is obtained by retracing the steps (C 3)–(C 7) in reverse. Thus, given A_j $(0 \leqslant j \leqslant N)$, we define

$$B_j = \tfrac{1}{2}\mathrm{e}^{-\mathrm{i}x_j}a_n + \tfrac{1}{2}\mathrm{i}\delta\mathrm{e}^{-\mathrm{i}x_j}A_{N-j} \quad (0 \leqslant j < N), \tag{C 8}$$

invert (C 6) for b_n in terms of B_j, and solve (C 5) for a_n.

The choice (C 5) for b_n is not unique; any expression of the form $b_n = \bar{a}_{2n} + c\bar{a}_{2n-1}$ with $c \neq \pm 1$ works. Also if use is made of the facts that $\cos(2n+1)x/\cos x$ and $\sin(2n+1)x/\sin x$ are expansible in finite series of terms $\cos 2px$, then the odd Fourier-transform algorithm can be dispensed with in favour of an even transform in the evaluation of (1.2) and its derivatives.

Appendix D. A model of vortex-sheet growth

In this appendix we describe a simple model for the inviscid growth of a vortex sheet which is qualitatively similar to the observed growth near the centre of the $y = 0$ face of the impermeable box. The crucial feature of the model is a variable convecting velocity field

$$v_z = \tfrac{1}{2}a(t)\sin 2z \tag{D 1}$$

describing convergence of fluid at $z = \frac{1}{2}\pi$, and a non-uniform convected velocity field satisfying

$$\frac{\partial v_x}{\partial t} + v_z\frac{\partial}{\partial z}v_x = 0 \tag{D 2}$$

with $v_x(z, t = 0) = \cos z$. Equation (D 2) follows upon making a boundary-layer-like approximation in the zone of convergence near $z = \frac{1}{2}\pi$ (see figure 2), after making a simple rotation to align this zone with the x-axis. From (D 2) it follows that

$$v_x(z, t) = v_x(z_0, 0) = \cos z_0, \tag{D 3}$$

where z is the solution of the differential equation $\mathrm{d}z/\mathrm{d}t = v_z$ with initial condition $z(t = 0) = z_0$. The solution $\tan z = \mathrm{e}^A \tan z_0$ with $A = A(t) = \int_0^t a(t')\,\mathrm{d}t'$ gives

$$v_x = \cos z(\cos^2 z + \mathrm{e}^{-2A}\sin^2 z)^{-\frac{1}{2}}. \tag{D 4}$$

For large times and z near $\frac{1}{2}\pi$ the vorticity is given by the strongly peaked and growing function

$$\omega_y \approx -\mathrm{e}^{-2A}[(z-\tfrac{1}{2}\pi)^2 + \mathrm{e}^{-2A}]^{-\frac{3}{2}}. \tag{D 5}$$

The width of the analyticity strip for this model solution is $\delta \approx \mathrm{e}^{-A}$, which, to the extent that $a(t)$ is only weakly dependent on time, varies exponentially with a halving time given by $T_{\frac{1}{2}} \approx (\ln 2)/a = \ln 2/|\nabla\cdot\boldsymbol{v}_{\parallel}|$.

REFERENCES

Baker, G. A. 1975 *Essentials of Padé Approximants*. Academic.

Baumel, R. T., Gammel, J. L. & Nuttall, J. 1981 *J. Comp. Appl. Maths* **7**, 135.

Benettin, G., Galgani, L. & Strelcyn, J. M. 1976 *Phys. Rev.* **A14**, 2338.

Caffarelli, L., Kohn, R. & Nierenberg, L. 1982 *Communs Pure Appl. Maths* **35**, 771.

Chang, Y. F., Tabor, M. & Weiss, J. 1982 *J. Math. Phys.* **23**, 531.

Chorin, A. J. 1981 *Communs Pure Appl. Maths* **34**, 853.

Fisher, M. E. & Au-Yang, M. 1979 *J. Phys.* A: *Math. & Gen.* **12**, 1677.

Fisher, M. E. & Au-Yang, M. 1980 *J. Phys.* A: *Math. & Gen.* **13**, 1517.

Frisch, U. 1983 Fully developed turbulence and singularities. In *Proc. Les Houches Summer School* 1981. North-Holland (to appear).

FRISCH, U., POUQUET, A., SULEM, P.-L. & MENEGUZZI, M. 1983 *J. Méc. Théor. Appl.* (to appear).

FRISCH, U., SULEM, P.-L. & NELKIN, M. 1978 *J. Fluid Mech.* **87**, 719.

FURTH, H. P., KILLEEN, J. & ROSENBLUTH, M. N. 1963 *Phys. Fluids* **6**, 459.

GRANT, H. L., STEWART, R. W. & MOILLIET, A. 1962 *J. Fluid Mech.* **12**, 241.

HÉNON, M. 1966 *C.R. Acad. Sci. Paris* **262**, 322.

HUNTER, D. L. & BAKER, JR, G. A. 1979 *Phys. Rev.* **B19**, 3808.

KAHANE, J. P. 1976 In *Turbulence and Navier–Stokes Equation* (ed. R. Temam). Lecture Notes in Mathematics, vol. 565, p. 94. Springer.

KOLMOGOROV, A. N. 1941 *C.R. Acad. Sci. USSR* **30**, 301.

KOLMOGOROV, A. N. 1962 *J. Fluid Mech.* **13**, 82.

KUO, A. Y. & CORRSIN, S. 1971 *J. Fluid Mech.* **50**, 285.

MANDELBROT, B. 1976 In *Turbulence and Navier–Stokes Equation* (ed. R. Temam). Lecture Notes in Mathematics, vol. 565, p. 121. Springer.

MONIN, A. S. & YAGLOM, A. M. 1975 *Statistical Fluid Mechanics*, vol. 2. M.I.T. Press.

MORF, R. H., ORSZAG, S. A. & FRISCH, U. 1980 *Phys. Rev. Lett.* **44**, 572.

MORF, R. H., ORSZAG, S. A., MEIRON, D. I., FRISCH, U. & MENEGUZZI, M. 1981 In *Proc. 7th Intl Conf. on Numerical Methods in Fluid Dynamics* (ed. R. W. MacCormack & W. C. Reynolds). Lecture Notes in Physics, vol. 141, p. 292. Springer.

ORSZAG, S. A. 1971 *Stud. Appl. Maths* **50**, 293.

ORSZAG, S. A. 1974 In *Proc. Symp. on Computing Methods in Applied Sciences and Engineering* (ed. R. Glowinski & J. L. Lions), part II, p. 50. Springer.

ORSZAG, S. A. 1976 In *Computer Science and Scientific Computing* (ed. J. Ortega), p. 191. Academic.

ORSZAG, S. A. 1977 Statistical theory of turbulence. In *Fluid Dynamics, Les Houches Summer School* 1973 (ed. R. Balian & J.-L. Peube), p. 237. Gordon & Breach.

SAFFMAN, P. G. 1971 *Stud. Appl. Maths* **50**, 377.

SCHEFFER, V. 1976 In *Turbulence and Navier–Stokes Equation* (ed. R. Temam). Lecture Notes in Mathematics, vol. 565, p. 174. Springer.

SIGGIA, E. 1981 *J. Fluid Mech.* **107**, 375.

SULEM, C., SULEM, P.-L. & FRISCH, H. 1983 *J. Comp. Phys.* (to appear).

TAYLOR, G. I. & GREEN, A. E. 1937 *Proc. R. Soc. Lond.* **A 158**, 499.

WOLIBNER, W. 1933 *Math. Z.* **37**, 698.